Computational and Applied Mathematics (2021) 40:70
https://doi.org/10.1007/s40314-021-01462-1

A nonlinear fourth-order PDE for image denoising in Sobolev spaces with variable exponents and its numerical algorithm

Hamdi Houichet[1,2] · **Anis Theljani**[3] · **Maher Moakher**[2]

Received: 21 May 2020 / Revised: 12 October 2020 / Accepted: 18 February 2021

Abstract

Image restoration is a very challenging task in image analysis and plays important roles in various fields such as medical imaging. In particular, in ultrasound imaging the obtained images are usually highly corrupted with multiplicative noise which makes important features hard to detect and to preserve. In this work, we use a mathematical model based on a minimization problem. To preserve the important features of the image, we consider a variable exponent function $p(x)$ chosen adaptively based on the map provided by edge-detectors which are constructed form high-order derivatives. The Euler–Lagrange equation of the minimization problem gives rise to a nonlinear $p(x)$-biharmonic PDE. We then propose a numerical scheme based on the convexity splitting (CS) method for the ultrasound image denoising and we prove its stability and convergence results. Finally, some numerical results are presented to illustrate the effectiveness of our approach.

Keywords $p(\cdot)$-Biharmonic equation · Variable exponent · Optimization procedures · Unconditionally stable scheme · Convexity splitting · Image denoising · Topological gradient · Structure tensor · Speckle noise

Mathematics Subject Classification 35R35 · 49J40 · 60G40

Communicated by Antonio C.G. Leitao.

✉ Hamdi Houichet
hamdi.houichet@gmail.com

Anis Theljani
thaljanianis@gmail.com

Maher Moakher
maher.moakher@enit.utm.tn

1 ESPRIT School of Engineering, Tunis, Tunisia

2 Laboratory for Mathematical and Numerical Modeling in Engineering Science, National Engineering School at Tunis, University of Tunis El Manar, B.P. 37, Belvédère, 1002 Tunis, Tunisia

3 University of Oxford, Oxford OX1 2JD, UK

Published online: 03 March 2021

1 Introduction

Image processing, such as denoising, edge detection and segmentation, plays an important role in various fields. In image restoration the goal is to reconstruct an original image from a degraded one. The objective of image denoising is to obtain a regularized version of a noisy or corrupted image. It is often a prerequisite for the successful use of classical image analysis algorithms. It is a challenging task in various fields (geophysics, optics, SAR imaging, medical imaging, etc.) and particularly in ultrasound medical imaging. In this work, we are interested in the restoration of images highly corrupted with multiplicative noise. Ultrasound images are strongly influenced by the quality of data usually corrupted with speckle noise (Houichet et al. 2019; Jin and Yang 2011; Krissian et al. 2005) which usually affects image analysis methods by making important features hard to detect. In the image denoising problem, we have an observed image, $f : \mathbb{R}^N \supset \Omega \to \mathbb{R}$ with $N \geq 2$, representing a real scene which is degraded and contaminated by a noise $\eta : \Omega \to \mathbb{R}$ and we aim to reconstruct an image $u : \Omega \to \mathbb{R}$ from f. The degradation model that we consider here is the following:

$$f = u + \sqrt{u}\eta, \tag{1}$$

where u is a positive function and η follows the Rayleigh distribution.

The reconstruction problem based on model (1) is an ill-posed inverse problem. Variational approaches are among the most successful methods to overcome the ill-posedness for such imaging problems by adding some prior regularization to the model (Bredies et al. 2010; Chan et al. 2000; Jin and Yang 2011; Rudin et al. 1992; Theljani 2020; Theljani et al. 2019). To reconstruct u, we impose the constraint that the solution must be smooth and intuitively we require that similar inputs should correspond to similar outputs. The problem then have a variational principal in which the optimization problem depends both on the regularization term (smoothness constraint) and the data fitting term (which depends on the noise $\eta = \dfrac{f-u}{\sqrt{u}}$).

One of the main issues to address is what is the “best” choice of the smoothness constrain to impose to smooth data, in a rather nonlinear way, without losing important image features such as points, filaments, edges, corners or other discontinuities. So far, many regularization schemes have been proposed in the literature such as the well-known total variation (TV) (Jin and Yang 2011; Rudin et al. 1992). However, it has been reported that TV-based methods yield staircasing artifacts in the restored images. There have been many efforts to improve the robustness and to reduce the staircasing effects of TV using the high-order TV and total generalized variation (TGV) regularizations (Bredies et al. 2010; Chan et al. 2000).

In this work, we consider the following minimization problem:

$$\min_{u>0,\, u\in X} \left\{ \int_\Omega \frac{1}{p(x)} |\Delta u|^{p(x)}\, \mathrm{d}x + \lambda \int_\Omega \frac{(f-u)^2}{u}\, \mathrm{d}x \right\} \tag{2}$$

subject to

$$\inf_{x\in\overline{\Omega}} f \leq u \leq \sup_{x\in\overline{\Omega}} f, \tag{3}$$

where $p(\cdot)$ is a given measurable continuous function satisfying $p(x) \in]1, 2]$ for all $x \in \Omega$. The first integral in (2) is the regularization term while the second one is the data fitting term. The positive constant λ is a weighting parameter.

The smoothness of the solution is driven by the variable exponent $p(\cdot)$ which will be chosen adaptively in a way to slow diffusion near important features of the image to sharpen and highlight them, and to enhance diffusion in homogeneous regions. The restoration task is carried out in two steps: in the first step, we use some edge detectors to effectively detect important features of the images. In the second step, we use the information furnished by the edge detector to build a varying exponent $p(\cdot)$ in the restoration process by considering the model (2) for $1 < p(x) \leq 2$.

This paper is organized as follows. In Sect. 2, we recall some basic notations and useful results of the generalized Lebesgue/Sobolev spaces. We prove, in Sect. 3, the well posedness of the minimization problem (2)–(3) and derive its associated Euler–Lagrange equation. In Sect. 4, we present the convexity splitting (CS) scheme and we prove its unconditional stability and convergence results. In Sect. 5, we present an adaptive strategy based on the topological gradient indicator and the structure tensor to choose the variable $p(x)$ and we present some numerical examples to test the efficiency and robustness of our proposed scheme.

2 Preliminaries for the generalized Sobolev spaces

For a bounded Lipschitz open set $\Omega \subset \mathbb{R}^N$, we assume that the variable-exponent function $p(\cdot) \in C(\overline{\Omega})$ satisfies the following condition:

$$1 < p^- := \inf_{x\in\overline{\Omega}} p(x) \leq p(x) \leq p^+ := \sup_{x\in\overline{\Omega}} p(x) \leq 2. \tag{P}$$

For any $x \in \overline{\Omega}$ we denote by $L^{p(\cdot)}(\Omega)$ the variable-exponent generalized Lebesgue space defined by

$$L^{p(\cdot)}(\Omega) = \left\{ u : \Omega \to \mathbb{R} \text{ measurable and } \int_\Omega \left| u(x) \right|^{p(x)} \mathrm{d}x < +\infty \right\},$$

which is equipped with the following norm:

$$\|u\|_{L^{p(\cdot)}(\Omega)} = \inf \left\{ \tau > 0 \,|\, \int_\Omega \left| \frac{u(x)}{\tau} \right|^{p(x)} \mathrm{d}x \leq 1 \right\}.$$

We recall that $(L^{p(\cdot)}(\Omega), \|\cdot\|_{p(\cdot)})$ is separable and reflexive Banach space (Fan and Zhao 2001).

For any $k \geq 1$, we denote by $W^{k,p(\cdot)}(\Omega)$ the variable-exponent generalized Sobolev space defined by

$$W^{k,p(\cdot)}(\Omega) = \{u \in L^{p(\cdot)}(\Omega) \,|\, D^\alpha u \in L^{p(\cdot)}(\Omega), |\alpha| \leq k\},$$

where $D^\alpha u = \frac{\partial^{|\alpha|}}{\partial x_1^{\alpha_1} \partial x_2^{\alpha_2} \cdots \partial x_N^{\alpha_N}} u$ with $\alpha = (\alpha_1, \alpha_2, \ldots, \alpha_N)$ is a multi-index and $|\alpha| = \sum_{i=1}^N \alpha_i$. The space $W^{k,p(\cdot)}(\Omega)$, which is equipped with the following norm:

$$\|u\|_{k,p(\cdot)} = \sum_{|\alpha|\leq k} \|D^\alpha u\|_{L^{p(\cdot)}(\Omega)},$$

is a separable and reflexive Banach space. For more background and proprieties of this kind of spaces, we refer the reader to Diening et al. (2011), Edmunds and Rákosník (2000), Fan and Zhao (2001).

Lemma 1 (Fan and Zhao 2001) *Let $p(x), r(x) \in C(\overline{\Omega})$. We have*

$$\text{if } 1 < p(x) \leq r(x) \text{ for } x \in \overline{\Omega}, \text{ then } L^{r(\cdot)}(\Omega) \hookrightarrow L^{p(\cdot)}(\Omega) \tag{4}$$

and the embedding is continuous.

In addition, the norm $\|\cdot\|_{2,p(\cdot)}$ is equivalent to the norm

$$\|u\| := \inf\left\{\tau > 0 \mid \int_\Omega \left|\frac{\Delta u(x)}{\tau}\right|^{p(x)} \mathrm{d}x + \int_\Omega \left|\frac{u(x)}{\tau}\right|^{p(x)} \mathrm{d}x \leq 1\right\},$$

in the spaces $W^{2,p(\cdot)}(\Omega)$ which is also equivalent to the norm $|\cdot|_{p(\cdot)} + |\Delta\cdot|_{p(\cdot)}$.

Remark 1 Ben Haddouch et al. (2016) If $2p(x) \geq \dim(\Omega)$ for all $x \in \overline{\Omega}$, then the set

$$W_{\mathbf{n}}^{2,\,p(\cdot)}(\Omega) = \left\{u \in W^{2,p(\cdot)}(\Omega) \text{ such that } \left.\frac{\partial u}{\partial \mathbf{n}}\right|_{\partial\Omega} = \left.\frac{\partial}{\partial \mathbf{n}}\left(|\Delta u|^{p(x)-2}\Delta u\right)\right|_{\partial\Omega} = 0\right\},$$

is a nonempty and closed subspace of $W^{2,p(\cdot)}(\Omega)$.

According to (Fan and Zhao 2001, Theorem 1.3), we have:

Proposition 1 *For any $u \in W^{2,p(\cdot)}(\Omega)$, we define the potential $\rho(u) = \int_\Omega |\Delta u|^{p(x)}\,\mathrm{d}x$. Then we have*

$$\begin{aligned} \|\Delta u\|^{p-}_{L^{p(\cdot)}(\Omega)} \leq \rho(u) \leq \|\Delta u\|^{p+}_{L^{p(\cdot)}(\Omega)}, \quad \text{if} \quad \|\Delta u\|_{L^{p(\cdot)}(\Omega)} \geq 1, \\ \|\Delta u\|^{p+}_{L^{p(\cdot)}(\Omega)} \leq \rho(u) \leq \|\Delta u\|^{p-}_{L^{p(\cdot)}(\Omega)}, \quad \text{if} \quad \|\Delta u\|_{L^{p(\cdot)}(\Omega)} \leq 1. \end{aligned}$$

Let us consider the following functional on $W_{\mathbf{n}}^{2,\,p(\cdot)}(\Omega)$:

$$J(u) = \int_\Omega \frac{1}{p(x)}|\Delta u|^{p(x)}\,\mathrm{d}x.$$

Lemma 2 *The functional J is continuously Fréchet differentiable on $W_{\mathbf{n}}^{2,\,p(\cdot)}(\Omega)$.*

Proof We note that $J(u)$ can be written as the composite functional $J(u) = Q(P(u))$ where $P(u) = \Delta u$ and $Q(u) = \int_\Omega \frac{1}{p(x)}|u|^{p(x)}\,\mathrm{d}x$. The functional Q is $C^1(W_{\mathbf{n}}^{2,\,p(\cdot)}(\Omega), \mathbb{R})$ and Fréchet differentiable (see Ciarlet et al. 2013; Amrouss and Ourraoui 2012; El Amrouss et al. 2009; Heidarkhani et al. 2016) and

$$\langle Q'(\varphi), h\rangle = \langle |\varphi|^{p(x)-1}\mathrm{sign}\,\varphi, h\rangle = \left\langle |\varphi|^{p(x)-1}\frac{\varphi}{|\varphi|}\varphi, h\right\rangle \quad \forall \varphi, h \in W_{\mathbf{n}}^{2,\,p(\cdot)}(\Omega).$$

Furthermore, the operator P is linear and hence is Fréchet differentiable at u and

$$P'(\psi)\cdot h = \Delta h, \qquad \forall h \in W_{\mathbf{n}}^{2,\,p(\cdot)}(\Omega).$$

Therefore, J is Fréchet differentiable at u and

$$\begin{aligned} \langle J'(\psi), \varphi\rangle_{\left(W_{\mathbf{n}}^{2,\,p(\cdot)}(\Omega)\right)', W_{\mathbf{n}}^{2,\,p(\cdot)}(\Omega)} &= \left\langle Q'(P(\psi)), P'(\psi)\cdot\varphi\right\rangle \\ &= \left\langle |\Delta\psi|^{p(x)-1}\frac{\Delta\psi}{|\Delta\psi|}, \Delta\varphi\right\rangle \\ &= \int_\Omega |\Delta\psi|^{p(x)-2}\Delta\psi\,\Delta\varphi\,\mathrm{d}x. \end{aligned}$$

Using Green's theorem and the boundary conditions satisfied by ψ and φ, we get

$$\langle J'(\psi), \varphi\rangle_{\left(W_{\mathbf{n}}^{2,\,p(\cdot)}(\Omega)\right)', W_{\mathbf{n}}^{2,\,p(\cdot)}(\Omega)} = \int_\Omega \Delta(|\Delta\psi|^{p(x)-2}\Delta\psi)\varphi\,\mathrm{d}x,$$

which means that

$$J'(\psi) = \Delta(|\Delta\psi|^{p(x)-2}\Delta\psi)$$

Now, we prove that J' is continuous. Fix $u \in W_{\mathbf{n}}^{2,\,p(\cdot)}(\Omega)$ and let $(u_n)_{n\geq 0} \in W_{\mathbf{n}}^{2,\,p(\cdot)}(\Omega)$ be a sequence such that $u_n \longrightarrow u$ as $n \longrightarrow +\infty$ in the space $(W_{\mathbf{n}}^{2,\,p(\cdot)}(\Omega), \|\cdot\|)$. The convergence of $(u_n)_{n\geq 0}$ to u in $(W_{\mathbf{n}}^{2,\,p(\cdot)}(\Omega), \|\cdot\|)$ implies that

$$\int_\Omega |\Delta u_n - \Delta u|^{p(x)} dx \longrightarrow 0, \quad \text{as } n \longrightarrow +\infty. \tag{5}$$

We also define the function $g : W_{\mathbf{n}}^{2,\,p(\cdot)}(\Omega) \longrightarrow L^{p'}$ by

$$g(u) = |\Delta u|^{p(x)-2}\Delta u.$$

Using the elementary inequality

$$\left||x|^{\gamma-2}x - |y|^{\gamma-2}y\right| \leq \beta|x-y|^{\gamma-1}, \quad \text{for all } x, y \in \mathbb{R}^N \text{ and } 1 < \gamma \leq 2$$

with β independent of x and y, we obtain

$$\|g(u_n) - g(u)\|_{L^{p'(x)}}^{p'(x)} \leq C \int_\Omega |\Delta u_n - \Delta u|^{p'(x)(p(x)-1)}. \tag{6}$$

Combining (5) and (6), we get that g is continuous. On the other hand, by the Holder's inequality

$$\begin{aligned}
\left|\left\langle J'(u_n) - J'(u), \varphi\right\rangle\right| &\leq \int_\Omega \left|g(u_n) - g(u)\right||\Delta\varphi|\,\mathrm{d}x \\
&\leq K\left(\int_\Omega \left|g(u_n) - g(u)\right|^{p'(x)}\right)^{\frac{1}{p'(x)}}\left(\int_\Omega |\Delta\varphi|^{p(x)}\,\mathrm{d}x\right)^{\frac{1}{p(x)}} \\
&\leq K\|g(u_n) - g(u)\|_{L^{p'(x)}}\|\varphi\|_{W^{2,p(x)}(\Omega)}
\end{aligned}$$

with $K > 0$ is constant independent of n, u_n, u and φ. Then we have

$$\|J'(u_n) - J'(u)\|_{\left(W_{\mathbf{n}}^{2,\,p(\cdot)}(\Omega)\right)'} \leq K\|g(u_n) - g(u)\|_{L^{p'(x)}}.$$

Using the continuity of g, we have $J'(u_n) \longrightarrow J'(u)$ as $n \longrightarrow +\infty$. Now, since J' is continuous, then the functional J is continuously Fréchet differentiable. $\square$

3 Existence and uniqueness of solution

The presence of the inequality constraint (3) makes the treatment of the minimization problem (2)–(3) hard. Motivated by the work (Hintermüller et al. 2011), we make use of a technique which replaces the inequality constraint by an equation. For this purpose, we transform the constrained optimization problem (2)–(3) into its Moreau–Yosida regularized version:

$$\min_{u>0,\, u\in W_{\mathbf{n}}^{2,\,p(\cdot)}(\Omega)} E_{p(\cdot)}(u), \tag{7}$$

where

$$E_{p(\cdot)}(u) := J(u) + \lambda \int_\Omega \frac{(f-u)^2}{u}\,\mathrm{d}x$$

$$+\frac{c}{2}\|\min(0, u-m)\|^2_{L^2(\Omega)} + \frac{c}{2}\|\max(0, u-M)\|^2_{L^2(\Omega)},$$

with $m := \inf_{x\in\Omega} f$, $M := \sup_{x\in\Omega} f$. Here, $0 < c \ll 1$ denotes the penalty parameter. Note that the constraint (3) has been relaxed to $u \in L^2(\Omega)$ by the min and max functions in the energy $E_{p(x)}$. Hence, in the limit $c \to 0$ we recover the original minimization problem (2). In the following proposition, we establish the well-posedness of (7).

Proposition 2 *Let $f \in W^{2,p(\cdot)}_{\mathbf{n}}(\Omega) \cap L^2(\Omega)$, the minimization problem (7) has a unique minimizer u in $W^{2,p(\cdot)}_{\mathbf{n}}(\Omega)$.*

Proof We start by proving the weak lower semi-continuity. We have

- The term $\|\min(0, u-m)\|^2_{L^2(\Omega)} + \|\max(0, u-M)\|^2_{L^2(\Omega)}$ is clearly convex w.r.t. u.
- The function $g(s) = \frac{(t-s)^2}{s}$ is strictly convex for all $s > 0$ as $g''(s) = \frac{2t^2}{s^3}$ for all $s > 0$. Thus the term $\lambda \int_\Omega \frac{(f-u)^2}{u}\,\mathrm{d}x$ is convex w.r.t. u
- The term $J(u)$ is clearly convex w.r.t. u.

Since the energy $E_{p(\cdot)}(u)$ is the sum of convex terms w.r.t u, then it is convex w.r.t. u. In addition, it is clear that $E_{p(\cdot)}(u)$ is a continuous function on the space $W^{2,p(\cdot)}_{\mathbf{n}}(\Omega)$. Therefore, the continuity and the strict convexity of $E_{p(\cdot)}(u)$ clearly imply that it is weakly lower semicontinuous.

Now, let $(u_n)_n \subset H(\Omega) := \{u > 0,\ u \in W^{2,p(\cdot)}_{\mathbf{n}}(\Omega)\}$ be a minimizing sequence of $E_{p(\cdot)}(u)$, i.e.,

$$E_{p(\cdot)}(u_n) \underset{n\to\infty}{\longrightarrow} \inf_{u\in W^{2,p(\cdot)}_{\mathbf{n}}(\Omega)} E_{p(\cdot)}(u).$$

Then there exists $C > 0$ such that

$$E_{p(\cdot)}(u_n) \le C. \tag{8}$$

Thus, $J(u_n) \le C$ and hence $\|\Delta u_n\|_{L^{p(\cdot)}(\Omega)}$ is uniformly bounded. It remains to prove that $\|u_n\|_{L^{p(\cdot)}(\Omega)}$ is uniformly bounded. Since

$$\int_\Omega |u_n|^2\,\mathrm{d}x = \int_{\{u_n<m\}} |u_n|^2\,\mathrm{d}x + \int_{\{u_n>M\}} |u_n|^2\,\mathrm{d}x + \int_{\{m\le u\le \overline{M}\}} |u_n|^2\,\mathrm{d}x,$$

from the inequality (8), we get

$$\int_\Omega \max(0, u_n-M)^2\,\mathrm{d}x = \int_{\{u_n>M\}} (u_n-M)^2\,\mathrm{d}x \le C,$$
$$\int_\Omega \min(0, u_n-m)^2\,\mathrm{d}x = \int_{\{u_n<m\}} (u_n-m)^2\,\mathrm{d}x \le C.$$

Thus, there exists $C_1 > 0$ such that

$$\int_{\{u_n<m\}} |u_n|^2\,\mathrm{d}x + \int_{\{u_n>M\}} |u_n|^2\,\mathrm{d}x \le C_1,$$

which implies

$$\int_\Omega |u_n|^2\,\mathrm{d}x \le C_1 + \int_{\{m\le u_n\le M\}} |u_n|^2\,\mathrm{d}x \le C_1 + M^2\mathrm{mes}(\{m \le u_n \le M\}).$$

Therefore, $(u_n)_n$ is uniformly bounded in $L^2(\Omega)$. Then, using (4) and the fact that $1 < p(\cdot) \le 2$, we get that $\|u_n\|_{L^{p(\cdot)}(\Omega)}$ is uniformly bounded. Thus, we obtain that $(u_n)_n$ is uniformly bounded in the Banach space $W_{\mathbf{n}}^{2,\,p(\cdot)}(\Omega)$, so it has a weakly convergent subsequence, still denoted $(u_n)_{n\in\mathbb{N}}$. Hence, there exists $u \in W_{\mathbf{n}}^{2,\,p(\cdot)}(\Omega)$ such that:

$$u_n \underset{n\to\infty}{\longrightarrow} u \text{ weakly in } W_{\mathbf{n}}^{2,\,p(\cdot)}(\Omega).$$

Using Fatou's Lemma and the weakly lower semi-continuity of $E_{p(\cdot)}(\cdot)$, we get

$$E_{p(\cdot)}(u) \le \liminf_{n\to\infty} E_{p(\cdot)}(u_n),$$

which implies that u is a solution of the minimization problem of (7).

The uniqueness of solution of the minimization problem (7) follows from the strict convexity of $E_{p(\cdot)}(u)$ for $u > 0$. □

The minimizer u of the functional $E_{p(\cdot)}$ satisfies the first optimality condition:

$$\Big\langle \nabla E_{p(\cdot)}(u), h \Big\rangle = 0, \tag{9}$$

for all $h \in W_{\mathbf{n}}^{2,\,p(\cdot)}(\Omega)$. Moreover, suing the derivative of $J(\cdot)$ in Lemma 2 and the derivative of the function $W_f(\cdot)$, we obtain:

$$\langle |\Delta u|^{p(x)-2}\Delta u, \Delta h\rangle_2 + \langle W_f'(u), h\rangle_2 = 0.$$

From the definition of the space $W_{\mathbf{n}}^{2,\,p(\cdot)}(\Omega)$ and using the Neumann boundary conditions of u, we have

$$\begin{cases} \Delta(|\Delta u|^{p(x)-2}\Delta u) + W_f'(u) = 0, & \text{in } \Omega, \\ \frac{\partial u}{\partial \mathbf{n}} = \frac{\partial}{\partial \mathbf{n}}\Big(|\Delta u|^{p(x)-2}\Delta u\Big) = 0, & \text{on } \partial\Omega. \end{cases} \tag{10}$$

To numerically solve the problem (9), we introduce an artificial time variable t and for any fixed number $T > 0$, we transform our problem to the following time-dependent one:

$$\begin{cases} u_t = -\nabla E_{p(\cdot)}(u), & \text{in } Q_T, \\ u(\cdot, t = 0) = f, & \text{in } \Omega, \end{cases} \tag{11}$$

where $Q_T = \Omega\times]0, T[$ and ∇ is interpreted as the variational derivative of $E_{p(\cdot)}(u)$ with respect to u. This leads to the PDE system

$$\begin{cases} u_t = -\Delta(|\Delta u|^{p(x)-2}\Delta u) - W_f'(u), & \text{in } Q_T, \\ u(., t = 0) = f, & \text{in } \Omega, \\ \frac{\partial u}{\partial \mathbf{n}} = \frac{\partial}{\partial \mathbf{n}}\big(|\Delta u|^{p(x)-2}\Delta u\big) = 0, & \text{on } \partial\Omega\times]0, T[. \end{cases} \tag{12}$$

Theorem 1 (Houichet et al. 2019) *Problem* (12) *admits a unique weak solution u, which satisfies:*

(i) $u \in L^\infty(0, T; L^2(\Omega)) \cap L^{p^-}(0, T; W_{\mathbf{n}}^{2,\,p(\cdot)}(\Omega))$, $\Delta u \in L^{p(\cdot)}(Q_T)$, $\partial_t u \in L^{p^-}(0, T; W_{\mathbf{n}}^{2,\,p(\cdot)}(\Omega)^*)$, $u(0) = f$.

(ii) *For any* $\phi \in L^\infty(0, T; L^2(\Omega)) \cap L^{p^-}(0, T; W_{\mathbf{n}}^{2,\,p(\cdot)}(\Omega))$, *we have*

$$\int_0^T \Big\langle \frac{\partial u}{\partial t}, \phi \Big\rangle \mathrm{d}t + \int_0^T \int_\Omega |\Delta u|^{p(x)-2}\Delta u \Delta\phi \,\mathrm{d}x\mathrm{d}t + \int_0^T \int_\Omega W_f'(u)\phi \,\mathrm{d}x\mathrm{d}t = 0.$$

(iii)

$$\|u\|_{L^\infty(0,T;L^2(\Omega))} + \left\|\frac{\partial u}{\partial t}\right\|_{L^{p^-}(0,T\ W_{\mathbf{n}}^{2,p(\cdot)}(\Omega)')} + \|u\|_{L^{p^-}(0,T;\ W_{\mathbf{n}}^{2,p(\cdot)}(\Omega))} \le C.$$

(iv) *Assume that* $f \in W_{\mathbf{n}}^{2,\,p(\cdot)}(\Omega) \cap L^\infty(\Omega)$ *with* $\inf_\Omega f > 0$. *Then* u *satisfies*

$$\inf_\Omega f < u(x,t) \le \sup_\Omega f, \text{ for a.e. } (x,t) \in Q_T. \tag{13}$$

4 Convexity splitting method

In this section, we present numerical algorithms that approximate solutions of the nonstandard higher order evolution equation (12) using the semi-implicit approach called convexity splitting (CS) method (Eyre 1998). Convexity splitting was originally proposed to solve general optimization problems (Yuille and Rangarajan 2003). It was, also, applied for more nonlinear PDEs like the Cahan–Hiliard and Ohta–Kawasaki models (Bertozzi and Schönlieb 2011; Kim and Shin 2017), and also for other applications (Elsey and Wirth 2013; Stuart and Humphries 1994). The main focus of this section is to illustrate the application of the convexity splitting strategy to (12).

Let $\Delta t = \frac{T}{K}$ denote the discrete time step with K an integer, and $t^k = k\Delta t$, with $k = 1, 2, \ldots, K$. Let $U^k(x) \approx u(x, t^k)$ denote an approximation of the solution obtained by the corresponding discrete-time numerical scheme of (12) at time t^k.

The basic idea of the convexity splitting is to split the functional $E_{p(\cdot)}$ into a convex part treated implicitly, and a concave one treated explicitly. In our case, we split the energy $E_{p(\cdot)}$ as follows:

$$E_{p(\cdot)} = E_{1,2} - E_{2,p},$$

where

$$\begin{cases} E_{1,2}(u) = \dfrac{c_1}{2}\displaystyle\int_\Omega |\Delta u|^2\,\mathrm{d}x + \dfrac{c_2}{2}\displaystyle\int_\Omega |u|^2\,\mathrm{d}x, \\ E_{2,p}(u) = -\displaystyle\int_\Omega \dfrac{1}{p(x)}|\Delta u|^{p(x)}\,\mathrm{d}x - \displaystyle\int_\Omega W_f(u)\,\mathrm{d}x + \dfrac{c_1}{2}\displaystyle\int_\Omega |\Delta u|^2\,\mathrm{d}x + \dfrac{c_2}{2}\displaystyle\int_\Omega |u|^2\,\mathrm{d}x, \end{cases}$$

and c_1 and c_2 are two positive constants.

Remark 2 The proposed model (12) is not defined for the degenerate case $\Delta u = 0$. Such singularity is avoided by perturbing the terms Δu with a small positive constant ϵ, to obtain

$$\int_\Omega \frac{1}{p(x)}|\Delta u|^{p(x)}\,\mathrm{d}x \approx \int_\Omega g_\epsilon(\Delta u)\,\mathrm{d}x, \tag{14}$$

where

$$g_\epsilon(\zeta) = \frac{1}{p(x)}(|\zeta|^2 + \epsilon^2)^{p(x)/2}.$$

We note that g_ϵ is convex in ζ, $g_\epsilon(\zeta) \to g(\zeta) = \frac{1}{p(x)}|\zeta|^{p(x)}$ as ϵ goes to 0 and the first derivative of the function g_ϵ is

$$G_\epsilon(\zeta) := (\epsilon^2 + |\zeta|^2)^{\frac{p(x)-2}{2}}\,\zeta.$$

In the numerical computation, the first term in $E_{2,p}$ is replaced by its regularized version, e.g. $\int_\Omega g_\epsilon(\Delta u)\,\mathrm{d}x$. To make sure that $E_{2,p}$ is strictly convex we assume that $c_1 > 2\epsilon^{p^- -2}$ and $c_2 > \lambda$.

For an initial data $U^0 = u(\cdot, 0)$, the first-order CS method is given by

$$\frac{U^{k+1} - U^k}{\Delta t} = -\nabla_{L^2(\Omega)}(E_{1,2}(U^{k+1}) - E_{2,p}(U^k)),$$

where ∇_{L^2} is the gradient with respect to the L^2-inner product. Thus,

$$\frac{U^{k+1} - U^k}{\Delta t} + c_1 \Delta\Delta U^{k+1} + c_2 U^{k+1} = -\Delta(G_\epsilon(\Delta U^k)) + c_1 \Delta^2 U^k + c_2 U^K - W_f'(U^k). \quad (15)$$

We use the Neumann boundary conditions, for all $x \in \Omega$ and $p \in]1, 2]$:

$$\frac{\partial U^k}{\partial \mathbf{n}} = \frac{\partial}{\partial \mathbf{n}}\left(G_\epsilon(\Delta U^k)\right) = 0. \quad (16)$$

In the case $p \equiv 2$, we can also use $\frac{\partial \Delta U^k}{\partial \mathbf{n}} = 0$ on the boundary $\partial\Omega$, for all $k = 1, 2, \ldots, K-1$. Moreover, from (13), we can assume that

$$m \le U^k(x) \le M, \quad \text{for all } k = 1, 2, \ldots, K-1. \quad (17)$$

In the following, we will prove that the scheme (15) is unconditionally stable.

Proposition 3 *The solution sequence $(U^k)_k$ is bounded on a finite time interval $[0, T]$ for all $\Delta t > 0$, and for $k\Delta t < T$ it fulfills*

$$\|\nabla U^k\|^2_{L^2(\Omega)} + \Delta t K_1 \|\nabla \Delta U^k\|^2_{L^2(\Omega)} \le e^{K_2 T}\left(\|\nabla f\|^2_{L^2(\Omega)} + \Delta t K_3 \|\nabla \Delta f\|^2_{L^2(\Omega)}\right), \quad (18)$$

where K_1, K_2 and K_3 are nonnegative constants.

Proof We multiply equation (15) by $-\Delta U^{k+1}$, integrate over Ω, apply Green's formula and use the boundary conditions (16), to obtain

$$\begin{aligned}\frac{1}{\Delta t}\left(\|\nabla U^{k+1}\|^2_{L^2(\Omega)} - \langle \nabla U^k, \nabla U^{k+1}\rangle_{L^2(\Omega)}\right) + c_1\|\nabla \Delta U^{k+1}\|^2_{L^2(\Omega)} + c_2 \|\nabla U^{k+1}\|^2_{L^2(\Omega)},\\ = -\langle G_\epsilon'(\Delta U^k)\nabla \Delta U^k, \nabla \Delta U^{k+1}\rangle_{L^2(\Omega)} + c_1 \langle \nabla \Delta u^k, \nabla \Delta U^{k+1}\rangle_{L^2(\Omega)}\\ + c_2\langle \nabla U^k, \nabla U^{k+1}\rangle - \langle W_f''(U^k)\nabla U^k, \nabla U^{k+1}\rangle_{L^2(\Omega)}.\end{aligned}$$

Furthermore, using Young's inequality, we have

$$\frac{1}{2\Delta t}\left(\|\nabla U^{k+1}\|^2_{L^2(\Omega)} - \|U^k\|^2_{L^2(\Omega)}\right) \le \frac{1}{\Delta t}\left(\|\nabla U^{k+1}\|^2_{L^2(\Omega)} - \langle \nabla U^k, \nabla U^{k+1}\rangle_{L^2(\Omega)}\right).$$

Then we obtain

$$\begin{aligned}\frac{1}{2\Delta t}\left(\|\nabla U^{k+1}\|^2_{L^2(\Omega)} - \|\nabla U^k\|^2_{L^2(\Omega)}\right) + c_1\|\nabla \Delta U^{k+1}\|^2_{L^2(\Omega)} + c_2\|\nabla U^{k+1}\|^2_{L^2(\Omega)}\\ \le \frac{1}{2}\|G_\epsilon'(\Delta U^k)\nabla\Delta U^k\|^2_{L^2(\Omega)} + \frac{1}{2}\|\nabla \Delta U^{k+1}\|^2_{L^2(\Omega)} + \frac{1}{2}\|W_f''(U^k)\nabla U^k\|^2_{L^2(\Omega)}\\ + \frac{1}{2}\|\nabla U^{k+1}\|^2_{L^2(\Omega)} + \frac{c_2}{2}\|\nabla U^k\|^2_{L^2(\Omega)} + \frac{c_2}{2}\|\nabla U^{k+1}\|^2_{L^2(\Omega)}. \quad (19)\end{aligned}$$

We recall that the function W_f is of class $\mathcal{C}^2$ on U^k for all $k = 1, 2, \dots, K-1$ and $W_f''(U^k) = 2\lambda \frac{f^2}{(U^k)^3}$. Thus, W_f'' is bounded and for all U^k satisfying (17), there exists a positive constant $c = 2\lambda M^2/m^3$ such that

$$\|W_f''(U^k)\nabla U^k\|^2_{L^2(\Omega)} \le c^2\|\nabla U^k\|^2_{L^2(\Omega)}. \tag{20}$$

On the other hand, from classical computation, we can see that for all s

$$G_\epsilon'(s) = \left(\epsilon^2 + |s|^2\right)^{\frac{p(x)}{2}-1}\left(\frac{(p(x)-2)s^2\operatorname{sign}(s)}{\epsilon^2+|s|^2} + 1\right).$$

Since $1 < p^- \le p(x) \le p^+$, we have

$$\begin{aligned}\frac{(p(x)-2)s^2\operatorname{sign}(s)}{\epsilon^2+|s|^2} + 1 &\le \left|\frac{(p(x)-2)s^2\operatorname{sign}(s)}{\epsilon^2+|s|^2}\right| + 1\\ &\le \frac{s^2}{\epsilon^2+|s|^2} + 1 \le 2.\end{aligned}$$

Thus, we have

$$|G_\epsilon'(s)| \le 2\left(\epsilon^2+|s|^2\right)^{\frac{p(x)}{2}-1} \le 2\epsilon^{p(x)-2}.$$

Moreover, since the function $y \longmapsto y-2$ is an increasing function, we have

$$|G_\epsilon'(s)| \le 2\epsilon^{p(x)-2} \le 2\epsilon^{p^+-2}.$$

Then for all $k \in \mathbb{N}$, it is easy to see that

$$\|G_\epsilon'(\Delta U^k)\nabla\Delta U^k\|^2_{L^2(\Omega)} \le 4\epsilon^{2p^+-4}\|\nabla\Delta U^k\|^2_{L^2(\Omega)}. \tag{21}$$

By plugging (20) and (21) in (19), we have

$$\begin{aligned}&\left(\frac{1}{2\Delta t} + \frac{c_2-1}{2}\right)\|\nabla U^{k+1}\|^2_{L^2(\Omega)} + \frac{c_1-1}{2}\|\nabla\Delta U^{k+1}\|^2_{L^2(\Omega)}\\ &\le \left(\frac{1}{2\Delta t} + \frac{c^2}{2} + \frac{c_2}{2}\right)\|\nabla U^k\|^2_{L^2(\Omega)} + \left(\frac{4\epsilon^{2p^+-4}}{2} + \frac{c_1}{2}\right)\|\nabla\Delta U^k\|^2_{L^2(\Omega)}.\end{aligned}$$

We multiply the above inequality by $2\Delta t$, to obtain

$$D_1\|\nabla u^{k+1}\|^2_{L^2(\Omega)} + D_2\|\nabla\Delta U^{k+1}\|^2_{L^2(\Omega)} \le D_3\|\nabla U^k\|^2_{L^2(\Omega)} + D_4\|\nabla\Delta U^k\|^2_{L^2(\Omega)}, \tag{22}$$

where

$$D_1 = 1 + \Delta t(c_2-1), \quad D_2 = (c_1-1), \quad D_3 = 1 + \Delta t(c^2+c_2), \quad D_4 = 4\epsilon^{2p^+-4} + c_1.$$

By choosing $c_2 > 1$, it gives $D_1 > 0$, we can divide (22) by D_1. Since c is greater than zero, then $\frac{D_3}{D_1}$ is greater than 1. We multiply the last term on the right side of the inequality by $\frac{D_3}{D_1}$, to get

$$\|\nabla U^{k+1}\|^2_{L^2(\Omega)} + \Delta t\frac{D_2}{D_1}\|\nabla\Delta U^{k+1}\|^2 \le \frac{D_3}{D_1}\left(\|\nabla U^k\|^2_{L^2(\Omega)} + \frac{D_4}{D_1}\|\nabla\Delta U^k\|^2_{L^2(\Omega)}\right).$$

By induction, we deduce that

$$\|\nabla U^k\|^2_{L^2(\Omega)} + \Delta t\frac{D_2}{D_1}\|\nabla\Delta U^k\|^2_{L^2(\Omega)} \le \left(\frac{D_3}{D_1}\right)^k\left(\|\nabla f\|^2_{L^2(\Omega)} + \Delta t\frac{D_4}{D_1}\|\nabla\Delta f\|^2_{L^2(\Omega)}\right),$$

$$\leq \left(\frac{1+\Delta t\tilde{D}_3}{1+\Delta t\tilde{D}_1}\right)^k \left(\|\nabla f\|^2_{L^2(\Omega)} + \Delta t\frac{D_4}{D_1}\|\nabla\Delta f\|^2_{L^2(\Omega)}\right),$$

where $\tilde{D}_3 = c^2 + c_2$ and $\tilde{D}_1 = c_2 - 1$. For $k\Delta t \leq T$, we have:

$$\begin{aligned}&\|\nabla u^k\|^2_{L^2(\Omega)} + \Delta t\frac{D_2}{D_1}\|\nabla\Delta U^k\|^2_{L^2(\Omega)}\\ &\leq \exp((c^2+1)T)\left(\|\nabla f\|^2_{L^2(\Omega)} + \Delta t\frac{D_4}{D_1}\|\nabla\Delta f\|^2_{L^2(\Omega)}\right).\end{aligned}$$

Then the estimate (18) holds and implies boundedness of the solution sequence on $[0, T]$ for any $T > 0$. □

To study the consistency of this convexity splitting scheme, we define the operator Δ^{-1}, which is the inverse of the negative Laplacian with homogeneous Neumann condition. More precisely, $u = \Delta^{-1}g$ is the unique solution of

$$\begin{cases}-\Delta u = g, & \text{in } \Omega,\\ \frac{\partial u}{\partial n} = 0 & \text{on } \partial\Omega.\end{cases}$$

The operator Δ^{-1} is defined the nonstandard space

$$\mathbf{H}^{-1}_\partial(\Omega) := \left\{\varphi \in H^1(\Omega)^* \text{ such that } \langle\varphi, 1\rangle_{(H^1)^*, H^1} = 0\right\},$$

where $H^1(\Omega)^*$ be the dual space of $H^1(\Omega)$.

where $H^1(\Omega)^*$ be the dual space of $H^1(\Omega)$. The inner product and the norm in $\mathbf{H}^{-1}_\partial(\Omega)$ will be written as

$$\langle\varphi, \psi\rangle_{-1} := \int_\Omega \nabla\Delta^{-1}\varphi\nabla\Delta^{-1}\psi\,\mathrm{d}x,$$

and norm

$$\|\varphi\|_{-1} := \sqrt{\int_\Omega (\nabla\Delta^{-1}\varphi)^2\,\mathrm{d}x}.$$

The space $\mathbf{H}^{-1}_\partial(\Omega)$ is closed in $H^1(\Omega)^*$, and, the norms $\|\cdot\|_{-1}$ and $\|\cdot\|_{-1}$ are equivalent on $\mathbf{H}^{-1}_\partial(\Omega)$.

We now proceed to the consistence result.

Proposition 4 *Let u_t be the solution of* (12) *and u the exact solution of* (12) *and $u^k = u(k\Delta t)$ be the exact solution at time $k\Delta t$ for a time step $\Delta t > 0$. If*

$$\|u_{tt}\|_{-1},\ \|\nabla\Delta u_t\|_{L^2(\Omega)} \text{ and } \|u_t\|_{L^2(\Omega)} \text{ are bounded,} \tag{23}$$

then the numerical scheme (15) *is consistent with the continuous equation* (12) *and is of order* 1 *in time.*

Proof We replace the discrete solution U of (15) by the exact solution u of (12). By subtracting (12) from (15) with the $p(x)$-biLaplace operator is approximated by (14), we have the local truncation error τ^k over a time step as

$$\tau^k = \frac{u^{k+1}-u^k}{\Delta t} + \Delta(G_\epsilon(\Delta u^k)) + \lambda W_f'(u^k) + c_1\Delta\Delta(u^{k+1}-u^k) + c_3(u^{k+1}-u^k) - \left(u_t(k\Delta t) + \Delta(G_\epsilon(\Delta u^k)) + W_f'(u^k)\right).$$

Thus,

$$\tau^k = \frac{u^{k+1}-u^k}{\Delta t} - u_t(k\Delta t) + c_1\Delta\Delta(u^{k+1}-u^k) + c_3(u^{k+1}-u^k). \tag{24}$$

Using standard Taylor series expansion arguments and the boundedness of $\|u_{tt}\|_{-1}$, $\|\nabla\Delta u_t\|_{L^2(\Omega)}$ and $\|u_t\|_{L^2(\Omega)}$, we have

$$\|\tau^k\|_{-1} = O(\Delta t). \tag{25}$$

□

It is important to study the convergence of the proposed scheme (15). For that, in the following proposition, we prove that the discrete solution converges to the continuous one as Δt goes to zero.

Proposition 5 (Convergence) *If the condition*

$$\|\nabla u^k\|^2_{L^2(\Omega)} + \|\nabla\Delta u^k\|^2_{L^2(\Omega)} \le C \text{ for a constant } C > 0, \text{ and for all } k\Delta t < T \tag{26}$$

holds, then the discretization error $e^k = u^k - U^k$ satisfies:

$$\|\nabla e^k\|^2 + \Delta t M_1\|\nabla\Delta e^k\|^2 \le T e^{2T} M_2,$$

where M_1, and M_2 are nonnegative constants.

Proof The idea of the proof is essentially the same as the previous proposition. For the readers' convenience and for completeness, we present it here.

From (24), we can write

$$\frac{u^{k+1}-u^k}{\Delta t} + c_1\Delta\Delta u^{k+1} + c_3u^{k+1} = -\Delta(G_\epsilon(\Delta u^k)) - W_f(u^k) + c_1\Delta\Delta u^k + c_3u^k + \tau^k. \tag{27}$$

Then $e^k = u^k - U^k$, for $k \in \mathbb{N}$, can be written as

$$\frac{e^{k+1}-e^k}{\Delta t} + c_1\Delta\Delta e^{k+1} + c_2e^{k+1} = -\Delta(G_\epsilon(\Delta u^k) + \Delta(G_\epsilon(\Delta U^k) + c_1\Delta\Delta e^k + c_2\Delta e^k + (W_f'(u^k) - W_f'(U^k)) + \tau^k. \tag{28}$$

We multiply (28) with $-\Delta e^{k+1}$ and integrate over Ω, to obtain

$$\begin{aligned}
&\frac{1}{\Delta t}\langle\nabla(e^{k+1}-e^k), \nabla e^{k+1}\rangle_2 + c_1\|\nabla\Delta e^{k+1}\|_2^2 + c_2\|\nabla e^{k+1}\|_2^2 \\
&= \langle\Delta(G_\epsilon(\Delta(u^k)) - \Delta(G_\epsilon(\Delta(U^k)), \Delta e^{k+1}\rangle_2 \\
&\quad - c_1\langle\Delta\Delta e^k, \Delta e^{k+1}\rangle_2 + c_2\langle\nabla e^k, \nabla e^{k+1}\rangle_2 \\
&\quad + \langle W_f''(u^k)\nabla u^k - W_f''(U^k)\nabla U^k, \nabla e^{k+1}\rangle_2 - \langle\tau^k, \Delta e^{k+1}\rangle_2.
\end{aligned}$$

Using Young's inequality, we have

$$\begin{aligned}
&\langle\Delta(G_\epsilon(\Delta u^k) - \Delta(G_\epsilon(\Delta U^k), \Delta e^{k+1}\rangle_2 \\
&\quad = -\langle G_\epsilon'(\Delta u^k)\nabla\Delta u^k - G_\epsilon'(\Delta U^k)\nabla\Delta U^k, \nabla\Delta e^{k+1}\rangle_2
\end{aligned}$$

$$
\begin{aligned}
&\le \frac{1}{2}\|G'_\epsilon(\Delta u^k)\nabla\Delta u^k - G'_\epsilon(\Delta U^k)\nabla\Delta U^k\|^2_{L^2(\Omega)} + \frac{1}{2}\|\nabla\Delta e^{k+1}\|^2_{L^2(\Omega)}\\
&\le \frac{4\epsilon^{2p^+-4}}{2}\left(\|\nabla\Delta u^k\|^2_{L^2(\Omega)} + \|\nabla\Delta U^k\|^2_{L^2(\Omega)}\right) + \frac{1}{2}\|\nabla\Delta e^{k+1}\|^2_{L^2(\Omega)}.
\end{aligned}
$$

Again using Young inequality and the above inequality, we have

$$
\begin{aligned}
&\frac{1}{2\Delta t}\left(\|\nabla e^{k+1}\|^2_{L^2(\Omega)} - \|\nabla e^k\|^2_{L^2(\Omega)}\right) + c_1\|\nabla\Delta e^{k+1}\|^2_{L^2(\Omega)} + c_2\|\nabla e^{k+1}\|^2_{L^2(\Omega)}\\
&\le \frac{4\epsilon^{2p^+-4}}{2}\left(\|\nabla\Delta u^k\|^2_{L^2(\Omega)} + \|\nabla\Delta U^k\|^2_{L^2(\Omega)}\right) + \frac{1}{2}\|\nabla\Delta e^{k+1}\|^2_{L^2(\Omega)} + \frac{c_1}{2}\|\nabla\Delta e^k\|^2_{L^2(\Omega)}\\
&+\frac{c_1}{2}\|\nabla\Delta e^{k+1}\|^2_{L^2(\Omega)} + \frac{c_2}{2}\|\nabla e^k\|^2_{L^2(\Omega)} + \frac{c_2}{2}\|\nabla e^{k+1}\|^2_{L^2(\Omega)} + \frac{1}{2}\|\tau^k\|^2_{-1}\\
&+\frac{1}{2}\|\nabla e^{k+1}\|^2_{L^2(\Omega)} + \frac{1}{2}\|W''_f(u^k)\nabla u^k - W''_f(U^k)\nabla U^k\|^2_{L^2(\Omega)} + \frac{1}{2}\|\nabla e^{k+1}\|^2_{L^2(\Omega)}.
\end{aligned}
$$

After reorganizing terms and using (20), we obtain

$$
\begin{aligned}
&\left(\frac{1}{2\Delta t} + \frac{c_2}{2} - 1\right)\|\nabla e^{k+1}\|^2_{L^2(\Omega)} + \left(\frac{c_1}{2} - \frac{1}{2}\right)\|\nabla\Delta e^{k+1}\|^2_{L^2(\Omega)}\\
&\le \left(\frac{1}{2\Delta t} + \frac{c_2}{2}\right)\|\nabla e^k\|^2_{L^2(\Omega)} + \frac{c_1}{2}\|\nabla\Delta e^k\|^2_{L^2(\Omega)}\\
&+\frac{2\epsilon^{2p^+-4}}{2}\left(\|\nabla\Delta u^k\|^2_{L^2(\Omega)} + \|\nabla\Delta U^k\|^2_{L^2(\Omega)}\right) + \frac{1}{2}\|\tau^k\|^2_{-1}\\
&+\frac{c^2}{2}\left(\|\nabla u^k\|^2_{L^2(\Omega)} + \|\nabla U^k\|^2_{L^2(\Omega)}\right).
\end{aligned}
$$

Next, we multiply this inequality by $2\Delta t$ and we divide by $B = 1 + \Delta t(c_2 - 2)$ to obtain

$$
\begin{aligned}
&\|\nabla e^{k+1}\|^2_{L^2(\Omega)} + \Delta t\frac{B_1}{B}\|\nabla\Delta e^{k+1}\|^2_{L^2(\Omega)} \le \frac{B_2}{B}\|\nabla e^k\|^2_{L^2(\Omega)} + \Delta t\frac{c_1}{B}\|\nabla\Delta e^k\|^2_{L^2(\Omega)} + \Delta t\frac{1}{B}\|\tau^k\|^2_{-1}\\
&+\Delta t\frac{B_3}{B}\left(\|\nabla U^k\|^2_{L^2(\Omega)} + \|\nabla\Delta U^k\|^2_{L^2(\Omega)} + \|\nabla u^k\|^2_{L^2(\Omega)} + \|\nabla\Delta u^k\|^2_{L^2(\Omega)}\right),
\end{aligned}
\tag{29}
$$

where

$$
B_1 = c_1 - 1,\qquad B_2 = 1 + \Delta t c_2 \quad\text{and}\quad B_3 = \max\left(4\epsilon^{2p^+-4}, c^2\right).
$$

By the uniform bound (18), the assumption (26) and the consistency result (25), the fact that $\frac{B_2}{B} \ge 1$, inequality (29) becomes

$$
\begin{aligned}
&\|\nabla e^{k+1}\|^2_{L^2(\Omega)} + \Delta t\frac{B_1}{B}\|\nabla\Delta e^{k+1}\|^2_{L^2(\Omega)} \le \frac{B_2}{B}\left(\|\nabla e^k\|^2_{L^2(\Omega)} + \Delta t\frac{c_1}{B}\|\nabla\Delta e^k\|^2\right)\\
&+\Delta t\left(\frac{1}{B}(\Delta t)^2 + \frac{B_3}{B}(C+K)\right).
\end{aligned}
$$

By induction on k, we deduce that

$$
\begin{aligned}
&\|\nabla e^k\|^2_{L^2(\Omega)} + 2\Delta t\frac{B_1}{B}\|\nabla\Delta e^k\|^2_{L^2(\Omega)}\\
&\le \left(\frac{B_2}{B}\right)^k\left(\|\nabla e^0\|^2_{L^2(\Omega)} + \Delta t\frac{c_1}{B}\|\nabla\Delta e^0\|^2_{L^2(\Omega)}\right) + \Delta t\sum_{i=0}^{k-1}\left(\frac{B_2}{B}\right)^i\left(\frac{1}{B}(\Delta t)^2 + (C+K)\right)
\end{aligned}
$$

$$\leq \Delta t \sum_{i=0}^{k-1} \left(\frac{1 + \Delta t c_2}{1 + \Delta t (c_2 - 2)} \right)^i \left(\frac{1}{B} O(\Delta t)^2 + (C + K) \right)$$

$$\leq \Delta t k \exp(2k\Delta t) \left(\frac{1}{B} O(\Delta t)^2 + (C + K) \right).$$

For $k\Delta t \leq T$, we finally have

$$\|\nabla e^k\|^2_{L^2(\Omega)} + \Delta t \frac{B_1}{B} \|\nabla \Delta e^k\|^2_{L^2(\Omega)} \leq T \exp(2T) M,$$

where $M = \frac{1}{B} O(\Delta t)^2 + (C + K)$. □

Remark 3 In practice, the assumptions (23) and (26) depend on the regularity of solutions u and u_t. They nevertheless seem to be reasonable in an heuristic sense if the initial data u_0 and the image f are smooth "enough", so they guarantee the regularity of solutions. However, clear and concrete theoretical result concerning this assumptions is still a matter for further research.

5 Numerical implementation

5.1 Adaptive strategy for the choice of $p(\cdot)$

The smoothness of solution of the minimization problem (7) is driven by the variable exponent $p(\cdot)$. To accurately detect features such as arteries, filaments, internal organ, corners, etc., we use must particular choices for variable exponent $p(\cdot)$. To meet this challenge, we employ the two methods which are described below:

Structure tensor The structure tensor (ST) describes the dominant direction in a local neighborhood of a specific point. ST encode local information on the image and can provide robust feature detection that has been used wide for low-level image processing steps (Baghaie and Zeyun 2015; Surya Prasath 2016; Prasath et al. 2015). The computations are performed based on a pixelwise method. ST has two important advantages. It can enhance the noise by the tensor product $T_0 = \nabla u \nabla u^t$, where ^{t} is the transposition operator, and it can capture local structures in the image and locate singularities. The smoothing is usually performed by convolution of the matrix components with a Gaussian kernel G_ρ with standard deviation ρ chosen empirically from the image for an optimal performance

$$T_\rho = G_\rho * (\nabla u \nabla u^t). \tag{30}$$

Here T_ρ is a field of bounded, symmetric, positive and semidefinite 2×2 matrices that contains in each element information on orientation and intensity of the surrounding structure of the image u. The tensor T_ρ has two eigenvectors which give the preferred local orientations, and the corresponding eigenvalues denoting the local contrast along these directions (Weickert and Scharr 2002). Furthermore, T_ρ can be written as:

$$T_\rho = PDP^{-1},$$

where $D = \text{diag}(\alpha_{\max}, \alpha_{\min})$ and $P = [T^1 \quad T^2]$ with $T^i = [T^i_x \quad T^i_y]^t$ for $i = 1$ (resp. $i = 2$) is the eigenvector associated with the eigenvalue $\alpha_{\max}$ (resp. $\alpha_{\min}$).

In flat regions (smooth regions), where the eigenvalues $\alpha_{\min} \approx \alpha_{\max} \approx 0$, variations are small and the region does not contain any edges. In regions where $\alpha_{\max} \gg \alpha_{\min} \approx 0$, there are a lot of variations and the current position represents an edge, a corner or a thin structure.

Note that, Gaussian smoothing not only improves the orientation information with respect to noise, but also creates a scale-space with scale parameter ρ. This scale parameter is crucial as it allows to determine the size of the neighborhood considered for the structure analysis. The higher ρ is, the smoother the T_ρ is. On the contrary, a low ρ ensures an accurate analysis but with high sensitive to noise.

In this work, the restoration task is provided by the proposed optimization problem and from this indicator we need only to detect the important objects, then we choose ρ very small. Further, we can improve the location of these objects using an adaptive choice of T_ρ at every iteration k. To update to exponent $p(\cdot)$, we use the following formula:

$$p(x) = 1 + \exp\left(-\mu\left|\arctan\left(\frac{T_x^1}{T_y^1}\right) + \frac{\alpha_{\max} - \alpha_{\min}}{\alpha_{\max} + \alpha_{\min}}\right|\right), \quad \forall x \in \Omega, \tag{31}$$

where $\mu > 0$ is a constant. It is worth noticing that the eigenvalues and eigenvectors of T_ρ are well adapted to discriminate different geometric features. The use of the eigenvalues and eigenvectors in (31) allows to automatically self-tune the local image structure in the gradient regularization term and will create a diffusion process in three different cases according to the three scales in the image, i.e., homogeneous regions, edges and thin structures:

1. $\alpha_{\min} \approx \alpha_{\max} \approx 0$: this case is associated with smooth regions of the image. In this case, $p(\cdot)$ is close to two. Then, the model (7) behaves like the classical biharmonic model which leads to strong diffusion and oscillations are damped.
2. $\alpha_{\max} \gg \alpha_{\min} \approx 0$: This case corresponds to the neighborhood of the edges. $\alpha_{\min}$ is very small and the term inside the absolute value in (31) is very important because the variation of the second eigenvalue $\alpha_{\max}$ is important (it detects both edges and thin structures). At this stage, $p(\cdot)$ is close to one and it leads to slow diffusion near the features of the image to keep them in the restoration process.
3. $\alpha_{\max} \geq \alpha_{\min} \gg 0$: This case is associated with the corners and the thin-features of the images. In this step the eigenvalues are high. Indeed, the variation of the first one will detect both edges and thin-structures, and the variation of second one will chiefly point to corners. Therefore, the exponent will also be close to 1, which in turn implies that corner points are not smoothed out. In addition, this case has the same impact on the detection of important features of image as the second case but $p(\cdot)$ decreases faster than the second case giving rise to a third level of diffusion.

The steps of the restoration algorithm are the following:

Algorithm 1 BASED ON THE STRUCTURE TENSOR

Given $U^0 = f$ and λ.
While $\|U^k - U^{k-1}\| > 10^{-4}$ **do**,

- Compute T_ρ using (30).
- Compute p using (31).
- Compute U^k using (15).

end.

Remark 4 In the cases where $\alpha_{\max}$ is much higher than $\alpha_{\min}$ or the two eigenvalues are higher than zero, this approach does not yield satisfactory results for the thin-structure and corner detection (Fillard et al. 2005). The most likely explanation lies in the particular geometry of the ST in the case of many images such as directional textures, tumor, veins, arteries, etc. Then the second step can not give good results for thin-structure detection. In Batchelor et al. (2005), Fillard et al. (2005), the authors proposed a "generalized" structure tensor by given a weight to the smallest eigenvalue $\alpha_{\min}$ which preserves the image contrast and mainly points to corners using the operator $T_\rho^\gamma = PD^\gamma P^{-1}$ where $\gamma \in]0, 1[$. In addition, this strategy deceases faster than the second case giving rise to a third level of diffusion (i.e., $\alpha_{\max} \geq \alpha_{\min} \gg 0$).

Here, to choose the optimal $p(\cdot)$ that preserves thin structures we propose a higher-order operator based on the fourth derivatives which allows us to localize points and all other important features of the image (Aubert and Drogoul 2015; Drogoul 2016; Houichet et al. 2019).

Topological gradient The goal of the topological gradient method is to decompose the image into several regions (Auroux 2009; Auroux and Masmoudi Nov 2008; Jaafar Belaid et al. 2008). The main idea of this method is as follows: if we insert a crack in a smooth part of the image, nothing happens. But, if we insert a crack along an edge or a corner, the energy decreases. Then important feature detection is equivalent to looking for sub-domains of Ω where the energy is small. Therefore, the starting point of this method is to insert a small artificial straight crack δ in the domain Ω and to minimize the energy norm J outside the important features, i.e., on $\Omega\backslash\delta_\varepsilon$, where $\delta_\varepsilon := \{x_0 + \varepsilon\delta(\mathbf{n})\}$ and $\mathbf{n} = [\cos\theta \quad \sin\theta]^t$ is a unit vector normal to the crack. After that, we measure the impact of such a modification of the domain on the cost function $\tilde{J}(u) = \int_{\Omega\backslash\delta_\varepsilon} |\Delta u|^2 \, dx$ (i.e., for fixed $p(\cdot) \equiv 2$) by computing the following asymptotic expansion as ε goes to zero, i.e.,

$$\lim_{\varepsilon\to 0} \frac{\tilde{J}(u_\varepsilon) - \tilde{J}(u)}{\varepsilon} = G(x_0, \mathbf{n}),$$

where u_ε is the solution of (10) for $p(\cdot) \equiv 2$ in the perturbed domain $\Omega\backslash\delta_\varepsilon$ and $G(x, \mathbf{n})$ is the topological gradient at the location x and orientation $\mathbf{n}$ of the crack given by Aubert and Drogoul (2015), Drogoul (2016), Houichet et al. (2019):

$$G(x, \mathbf{n}) = -\tfrac{2\pi}{3}\nabla^2 u(x)(\mathbf{n}, \mathbf{n})\nabla^2 v(x)(\mathbf{n}, \mathbf{n}), \tag{32}$$

with u is a solution of (10) for $p(\cdot) \equiv 2$ in Ω and v is the solution of the following adjoint problem

$$\begin{cases} \Delta^2 v + W_f''(u)v = -\Delta^2 u, & \text{in } \Omega, \\ \frac{\partial \Delta v}{\partial \mathbf{n}} = \frac{\partial v}{\partial \mathbf{n}} = 0, & \text{on } \partial\Omega. \end{cases} \tag{33}$$

In practice, we use the splitting convexity scheme to iteratively solve system

$$\Delta^2 v^{n+1} + cv^{n+1} = -\Delta^2 u - W_f''(u)v^n - cv^n, \text{ in } \Omega,$$

where $c > 0$. To solve the above fourth-order equations in each time step iteration, we use the two-dimensional discrete Fourier transforms. Applying the Fourier transform, we write

$$\mathcal{F}[\Delta^2 v^{n+1}] + c\mathcal{F}[v^{n+1}] = -\mathcal{F}[\Delta^2 u] - \mathcal{F}[W_f''(u)v^n - cv^n].$$

Thus, we have

$$L \odot \mathcal{F}(V) = -\mathcal{F}[\Delta^2 u] - \mathcal{F}[W_f''(u)v^n - cv^n],$$

where $L = \mathcal{F}(\Delta^2\cdot) + cI_d$., the operator $\mathcal{F}(\cdot)$ is the Fourier transform and "$\odot$" means pointwise multiplication of matrices. Therefore, for each iteration $n > 0$

$$v^{k+1} = \mathcal{F}^{-1}\left(-\mathcal{F}[\Delta^2 u] - \mathcal{F}[W_f''(u)v^n - cv^n]/(\mathcal{F}(\Delta^2\cdot) + cI_d)\right), \tag{34}$$

where "$/$" means point-wise division of matrices. We noticed that the above iterative iterations need only few iteration (less than 15) to converge.

The smoothness of solution of the minimization problem (7) is driven by the variable exponent $p(x)$. The selection of $p(\cdot)$ is performed with the help of the topological gradient which has been used as an efficient edge- and thin structure-detector. This particularity makes it well suited to control and locally select the exponent using the following algorithm:

Algorithm 2 BASED ON THE TOPOLOGICAL GRADIENT

Given $U^0 = f, \lambda$.
Initialize $p \equiv 2$,

- Compute U^k and v using (15) and (34), respectively.
- Compute $G(x, \mathbf{n})$ using (32) and update p using

$$p(x) = 1 + \exp(-\mu |G(x, \mathbf{n})|), \ \forall x \in \Omega. \tag{35}$$

While $\|U^k - U^{k-1}\| > 10^{-4}$ **do**

- Compute U^k using (15).

end.

Remark 5 In homogeneous regions, we have $G(x, \mathbf{n}) \approx 0$ leading to a new exponent $p(x)$ (35) close to 2. Then, the model behaves like the biharmonic equation leading to strong diffusion and hence noise is damped. Near edges/thin-structures, $G(x, \mathbf{n})$ is very important and therefore $p(x)$ will be close to 1 which slows down diffusion.

In this algorithm, we do not need to use an adaptive choose of $p(\cdot)$ at every iteration as the ST. Because the topological gradient is known as a one shot algorithm for edges detector (Auroux and Masmoudi 2006).

5.2 Numerical experiments

To achieve quantitative comparison, we considered gray-value images and the quality of the restored image is measured by the Signal-to-Noise Ratio (SNR), Peak Signal-to-Noise Ratio (PSNR) and the Structural Similarity Index Measurement (SSIM). We set $\epsilon = 10^{-4}$, $c_1 = 30$, $\lambda = 15$, $c_2 = 20$, $\rho = 0.02$ and $\Delta t = 0.1$. The numerical results demonstrate the ability of our algorithms to denoise the images as well as the detection of thin-structures and edges. All algorithms were implemented in Matlab 9.4 (R2018a) running on a Desktop with Intel core i7 processor, CPU at 3.4 GHz and 8GB RAM memory. We first compare our model with the following models:

- Total Laplacian model (TL) :

$$\min_{\{u>0\}} \int_\Omega |\Delta u| \mathrm{d}x + \lambda \int_\Omega W_f(u)\, \mathrm{d}x.$$

- Total variation model (TV):

$$\min_{\{u>0\}} \int_\Omega |\nabla u| \mathrm{d}x + \lambda \int_\Omega W_f(u)\, \mathrm{d}x.$$

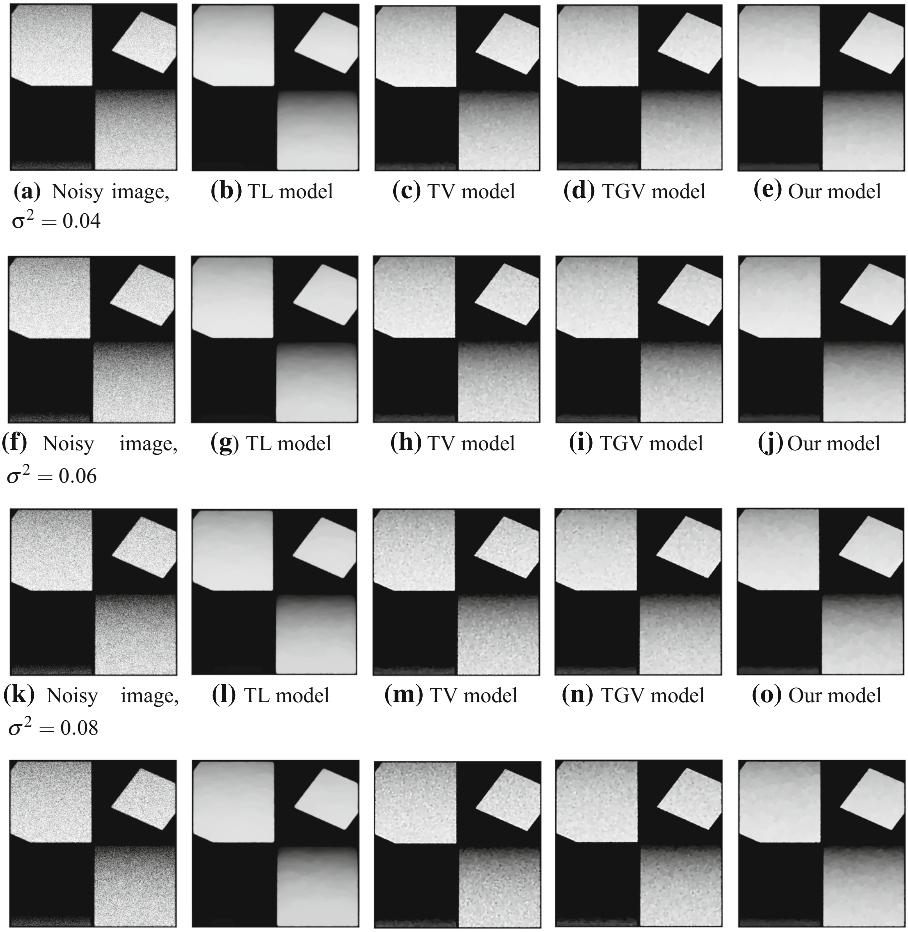

(a) Noisy image, $\sigma^2 = 0.04$ **(b)** TL model **(c)** TV model **(d)** TGV model **(e)** Our model

(f) Noisy image, $\sigma^2 = 0.06$ **(g)** TL model **(h)** TV model **(i)** TGV model **(j)** Our model

(k) Noisy image, $\sigma^2 = 0.08$ **(l)** TL model **(m)** TV model **(n)** TGV model **(o)** Our model

(p) Noisy image, $\sigma^2 = 0.1$ **(q)** TL model **(r)** TV model **(s)** TGV model **(t)** Our model

Fig. 1 From left to right and top to bottom: The noisy image for different noise level, the restored image using the TL model, the restored image using the TGV model, the restored image using the TV model and the restored image using our proposed model, respectively

– Second-order Total Generalized Variation (TGV):

$$\min_{\{u>0\}} TGV_\alpha^2(u) + \lambda \int_\Omega W_f(u)\, \mathrm{d}x,$$

where $TGV_\alpha^2(u) = \sup\{\int_\Omega u \mathrm{div}^2 v \,\mathrm{d}x \mid v \in C_c^2(\Omega, \mathrm{Sym}^2(\mathbb{R}^2)),\ \|\mathrm{div}^i v\| \leq \alpha_i,\ i = 0, 1\}$.

In Figs.1 and 2, we demonstrate the effectiveness of the proposed model applied to three noisy synthetic images corrupted with different noise levels σ. We can see that our model delivers better image quality than the competitive models. For example, for a noise level $\sigma^2 = 0.1$, the restored image using TL model in Fig. 1q is very blurred. Moreover, it is visually clear that the restored images using TGV and TV models are still noisy (see Fig. 1r,

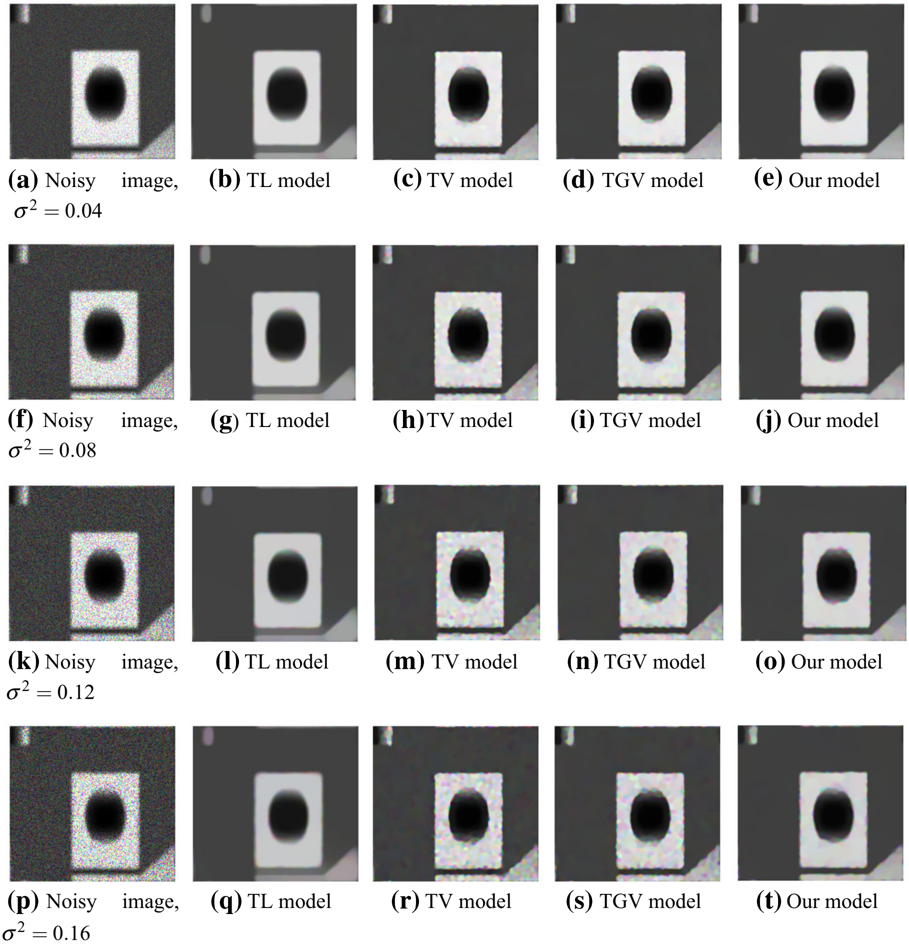

(a) Noisy image, $\sigma^2 = 0.04$ **(b)** TL model **(c)** TV model **(d)** TGV model **(e)** Our model

(f) Noisy image, $\sigma^2 = 0.08$ **(g)** TL model **(h)** TV model **(i)** TGV model **(j)** Our model

(k) Noisy image, $\sigma^2 = 0.12$ **(l)** TL model **(m)** TV model **(n)** TGV model **(o)** Our model

(p) Noisy image, $\sigma^2 = 0.16$ **(q)** TL model **(r)** TV model **(s)** TGV model **(t)** Our model

Fig. 2 From left to right and top to bottom: The noisy image for different noise level, the restored image using the TL model, the restored image using the TGV model, the restored image using the TV model and the restored image using our proposed model, respectively

Table 1 Comparison between all models for Fig 1using the SSIM and PSNR indicators

		Noisy image	Our model	TGV model	TV model	TL model
$\sigma = 0.04$	SSIM	0.4345	0.946	0.944	0.924	0.795
	PSNR	18.943	27.871	27.856	27.418	24.242
$\sigma = 0.06$	SSIM	0.420	0.943	0.924	0.881	0.77
	PSNR	17,658	26.828	26.603	26.53	23.761
$\sigma = 0.08$	SSIM	0.412	0.941	0.901	0.847	0.769
	PSNR	16.685	25.834	25.615	25.467	23.312
$\sigma = 0.1$	SSIM	0.406	0.938	0.8771	0.81	0.763
	PSNR	15.916	25.104	24.916	24.348	22.854

Table 2 Comparison between all models for Fig. 2 using the SSIM and PSNR indicators

		Noisy image	Our model	TGV model	TV model	TL model
$\sigma = 0.04$	SSIM	0.32	0.909	0.904	0.902	0.872
	PSNR	20.039	25.346	25.332	24.472	21.022
$\sigma = 0.08$	SSIM	0.225	0.895	0.88	0.861	0.865
	PSNR	17,92	23.568	23.299	23.17	20.132
$\sigma = 0.12$	SSIM	0.179	0.882	0.849	0.825	0.851
	PSNR	16.484	22.234	22.13	22.007	19.48
$\sigma = 0.16$	SSIM	0.152	0.872	0.816	0.781	0.847
	PSNR	15.431	21.13	21.106	21.033	18.808

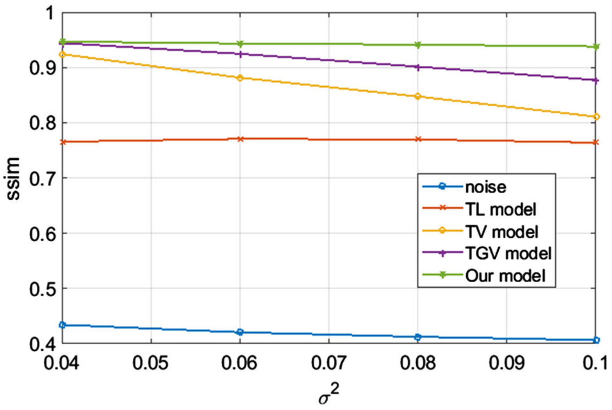

Fig. 3 Comparison between the presented models using the SSIM indicator in Table 1

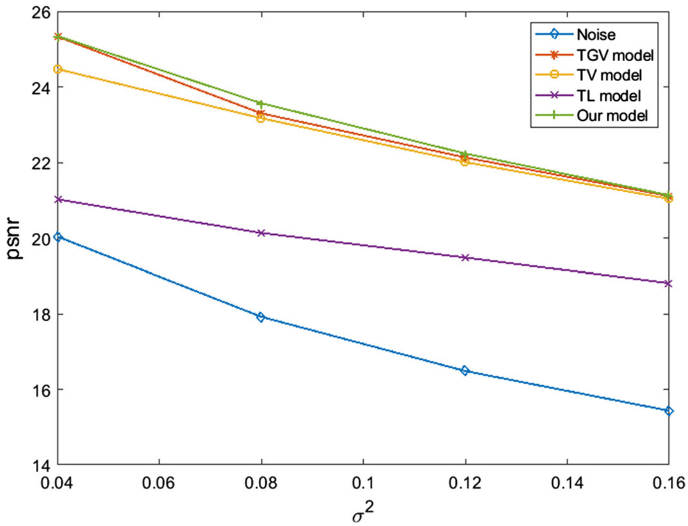

Fig. 4 Comparison between the presented models using the PSNR indicator in Table 2

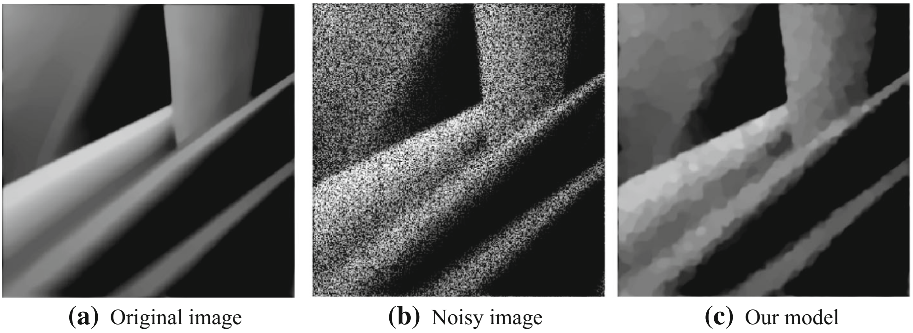

Fig. 5 From left to right: the original image, the noisy one with noise level $\sigma^2 = 0.16$ and restored image using our model, respectively

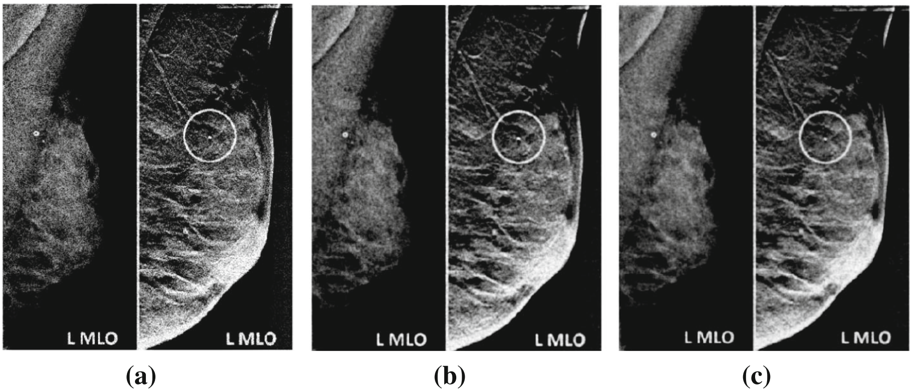

Fig. 6 From left to right: **a** noisy image, **b** restored image using Algorithm 1, **c** restored image using Algorithm 2

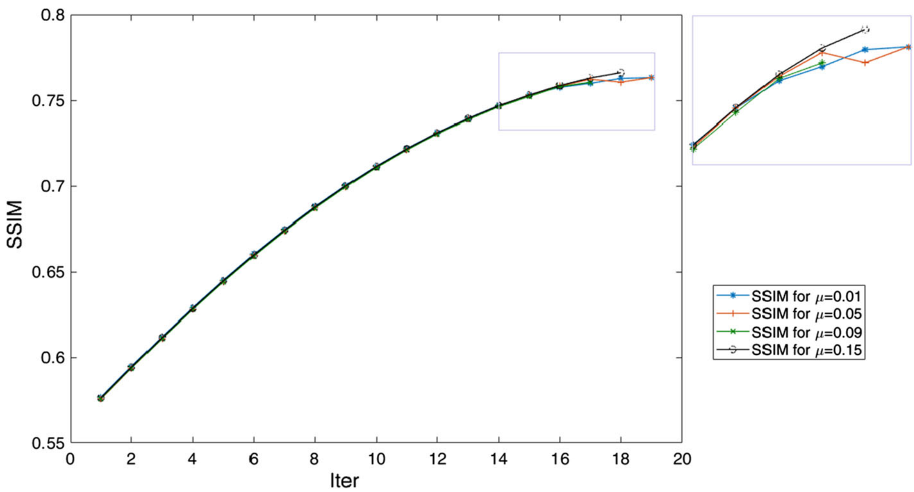

Fig. 7 The iterations number as a function of the SSIM index of the restored images using Algorithm 1 for different values of μ of Fig. 6

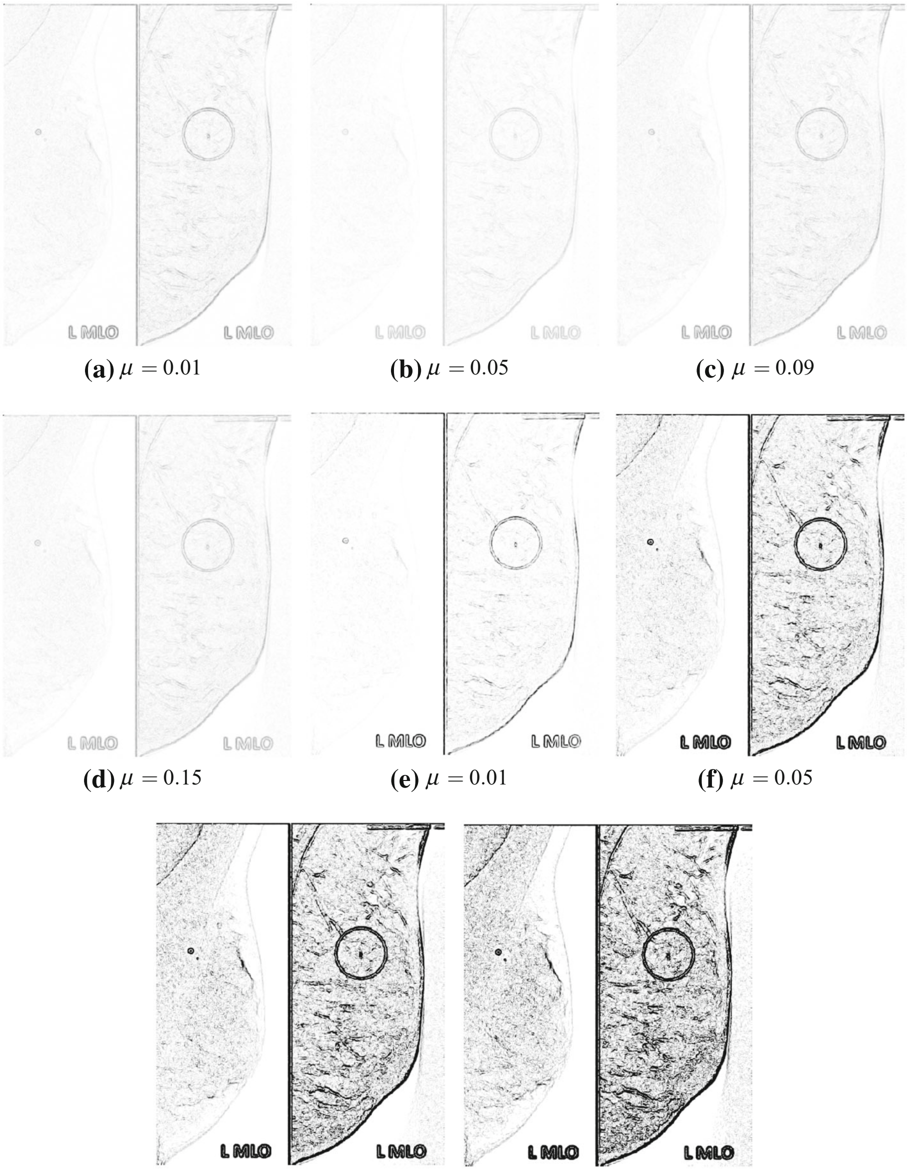

(a) $\mu = 0.01$ (b) $\mu = 0.05$ (c) $\mu = 0.09$

(d) $\mu = 0.15$ (e) $\mu = 0.01$ (f) $\mu = 0.05$

(g) $\mu = 0.09$ (h) $\mu = 0.15$

Fig. 8 The map provided by the exponent $p(\cdot)$ using classical gradient detector and the topological gradient indicator, respectively, for different values of μ

s). However, we can see that the noise is effectively removed using our model (see Fig. 1t). The comparison between all models for these two examples is summarized in Table 1 and Table 2.

In Figures 3 and 4, we give the curves of the SSIM and the PSNR values for all models as functions of the different values of noise level. It is clear that our model outperforms all

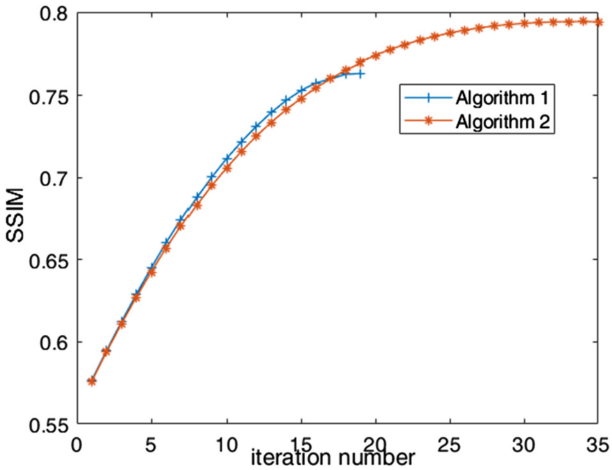

Fig. 9 Iteration number as a function of the SSIM index of the restored images in Fig. 6

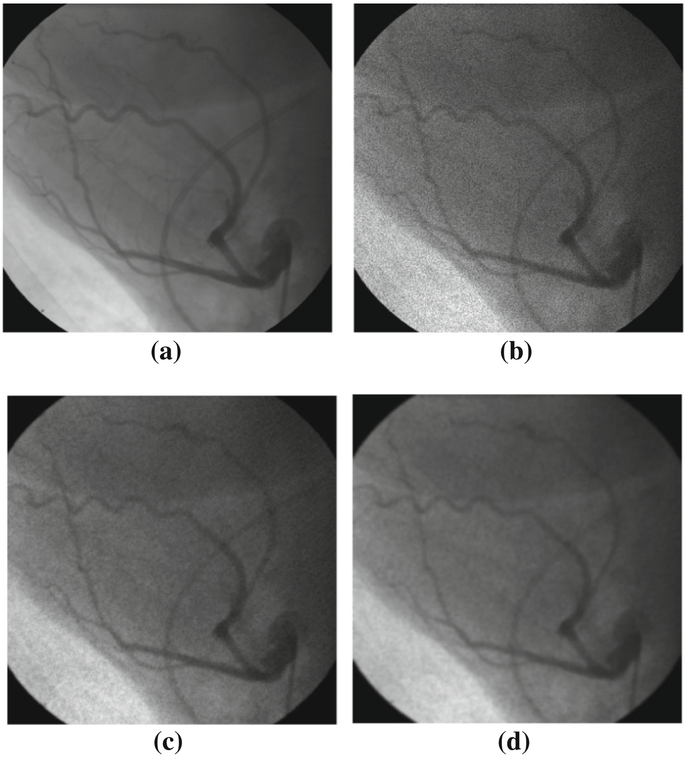

Fig. 10 From left to right and top to left: **a** original image **b** noisy image, **c** restored image using Algorithm 1, **d** restored image using Algorithm 2

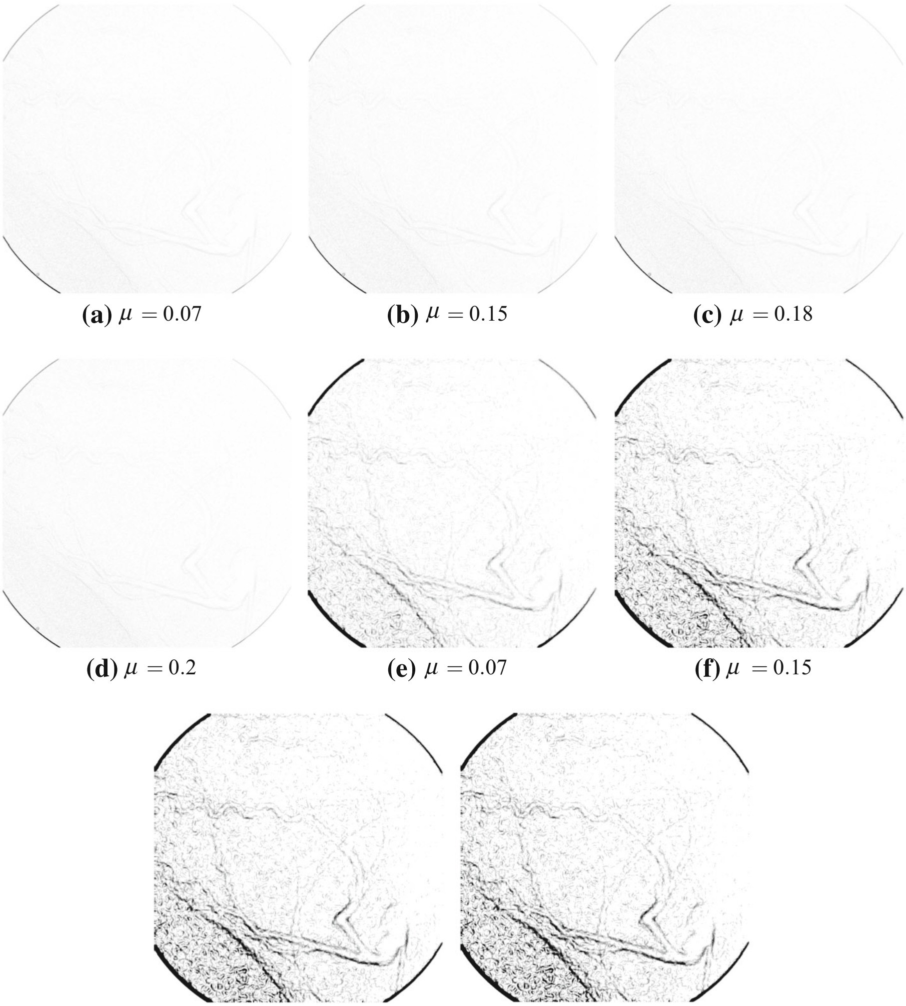

(a) $\mu = 0.07$ **(b)** $\mu = 0.15$ **(c)** $\mu = 0.18$

(d) $\mu = 0.2$ **(e)** $\mu = 0.07$ **(f)** $\mu = 0.15$

(g) $\mu = 0.18$ **(h)** $\mu = 0.2$

Fig. 11 The map provided by the exponent $p(\cdot)$ using classical gradient detector and the topological gradient indicator for different values of μ

other models. For example, the curve of SSIM of our model does not drop below 0.9 unlike the other models, which means that our model is stable.

5.2.1 Comparison between the algorithms 1 and 2

First, we compare the SSIM of the restored images using Algorithm 1 at different values of μ in (31). We choose here a breast cancers image (Fig. 8) which is degraded by speckle noise with variance $\sigma^2 = 0.06$. The SSIM values using the different μ look visually similar. The main diSSIMilarity is highlighted by zooming in the extreme part of the SSIM curve where it is clear that for iterations < 14, the four values of μ are broadly comparable. However, the advantages of the different values can be seen for iterations > 14 (Fig. 7).

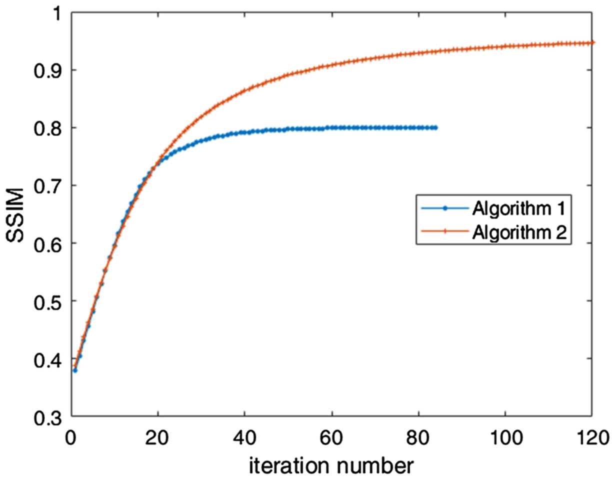

Fig. 12 Iteration number as a function of the SSIM index of the restored images in Fig. 10

In Fig. 8, we show the segmented regions of the noisy image in Fig. 6 at different values of μ using (31) and (35). We can show that the map provided by (35) which are obtained using the topological gradient (32) are more effective than those obtained using the ST (30). Hence, we can show that tumors, cancers and the thin structures (singularities) are well located using the topological gradient indicator. We can show that the ST can enhance the smooth regions of the image but it is not the case for the topological gradient indicator. Furthermore, in Fig. 6, we compare the restored images using the Algorithms 1 and 2. We show that Algorithm 2 is able to remove the staircase artifacts while it preserves the important features of the images. We can also see, in Fig. 9, that Algorithm 2 outperforms Algorithm 1 in the sense that the SSIM index for the second algorithm reach 0.79 after 35 iterations compared with the first algorithm in the extremum value of the SSIM is 0.76 which attained after only 19 iterations.

In Fig. 5, we test the performance of the proposed for high level of noise, i.e. $\sigma^2 = 1.6$. The restore image in Fig. 5c shows that our model is robust for important noise level. In fact. the noise is well removed and the important features are preserved.

To show the performance of the ST and the topological gradient for the segmentation of thin objects and points which have a width no greater than few pixels (have very elongated dimensions compared with the image, see, e.g., Fig. 10a). In Figs. 11 and 10, we show the segmented images and the restored ones using the two algorithms, respectively. We consider in Fig. 10b a noisy image with noise level $\sigma^2 = 0.04$. We can see that the segmentation results obtained by the topological gradient indicator are better than the segmented results by the ST. Also, the important features of image are well captured by the exponent $p(x)$ map and thus preserved by controlling the diffusion in Fig. 10d. The main difference between the results are presented on Fig. 12. We show that the SSIM index of the result by second algorithm highlights the SSIM result of the first algorithm.

Figure 13 represents the map provided by the ST and the topological gradient one can see that a good segmentation and homogeneous zones and a bad curves detection by the ST and not the case for the topological gradient which is able to detect the curves and the textures.

In Fig. 14, we show that our proposed model is able to remove noise while important features (edges and corners, etc.) are well preserved.

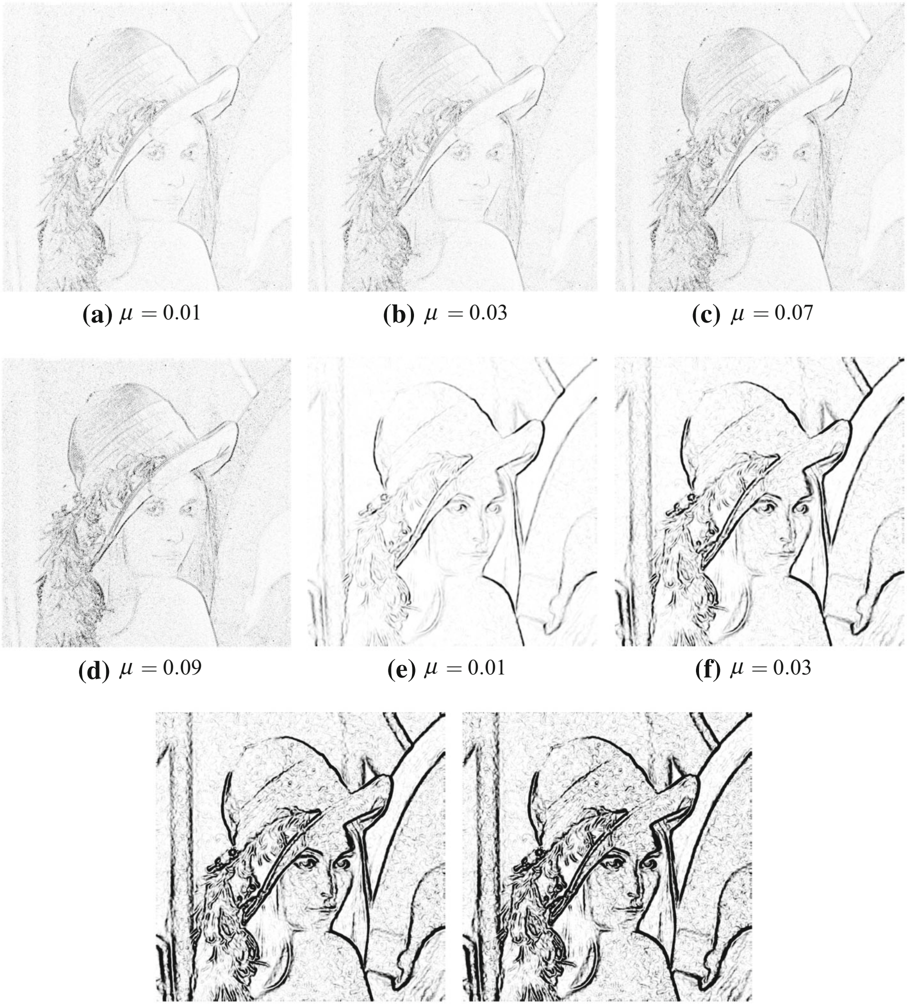

(a) $\mu = 0.01$ **(b)** $\mu = 0.03$ **(c)** $\mu = 0.07$

(d) $\mu = 0.09$ **(e)** $\mu = 0.01$ **(f)** $\mu = 0.03$

(g) $\mu = 0.07$ **(h)** $\mu = 0.09$

Fig. 13 The map provided by the exponent $p(\cdot)$ using classical gradient detector and the topological gradient indicator for different values of μ

The performance of our proposed algorithms are compared quantitatively using the SNR, PSNR, SSIM and CPU indicators which are summarized in Table 3.

6 Conclusion

In this paper, we have presented a new scheme for the restoration and segmentation of images corrupted by speckle noise based on the convexity splitting method. The proposed approach combines the advantages of the topological gradient indicator and the structure tensor for important feature detection and the anisotropic diffusion model based on the

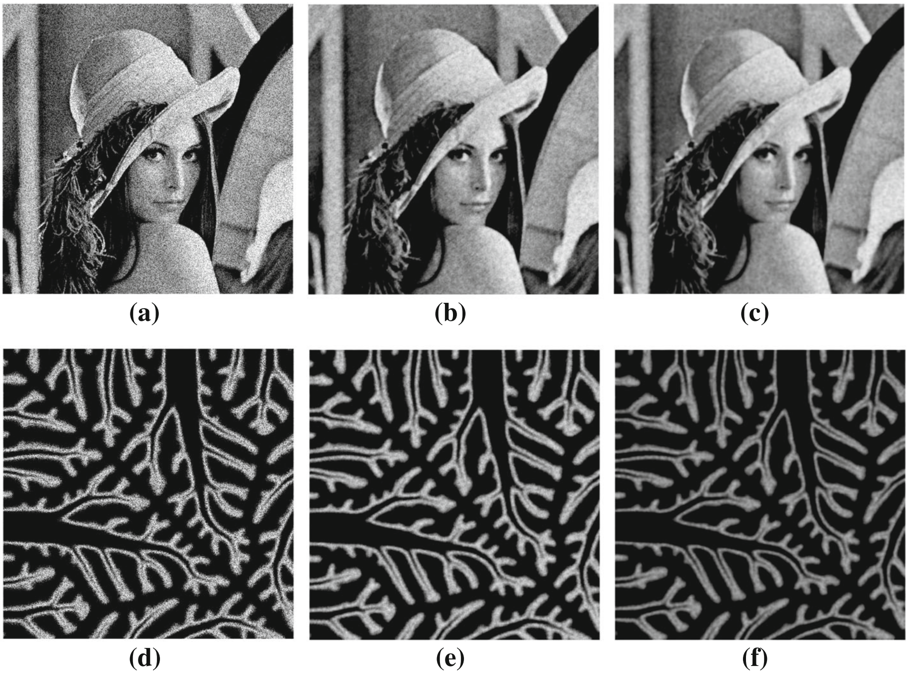

Fig. 14 From left to right and top to bottom: original image, noisy image, restored image, respectively

Table 3 Table for comparison of results of gray-scale images in Figs. 6, 10 and 14

Image		Noisy image	Algorithm 1	Algorithm 2
Breast cancers	SSIM	0.558	0.766	0.794
	PSNR	21.268	25.89	26.604
	SNR	12.821	17.07	18.093
	CPU (s)		4.884	17.964
Coronary vessels	SSIM	0.356	0.794	0.946
	PSNR	20.507	22.959	24.956
	SNR	10.962	14.89	18.668
	CPU (s)		33.469	64.193
Monochrome	SSIM	0.437	0.762	0.913
	PSNR	21.576	27.319	31.567
	SNR	12.47	19.406	22.088
	CPU (s)		24.156	50.727
Lena	SSIM	0.317	0.678	0.772
	PSNR	19.758	27.92	28.356
	SNR	14.252	21.323	22.64
	CPU (s)		22.636	53.213

exponent function $p(\cdot)$ for the denoising/segmentation. The numerical experiments show the good results in the recovering of the thin structures as well as the image denoising.

References

Aubert G, Drogoul A (2015) Topological gradient for a fourth order operator used in image analysis. ESAIM Control Optim Calc Variat 21(4):1120–1149

Auroux D (2009) From restoration by topological gradient to medical image segmentation via an asymptotic expansion. Math Comput Model 49(11):2191–2205

Auroux D, Masmoudi M (2006) A one-shot inpainting algorithm based on the topological asymptotic analysis. Computat Appl Math 25(2–3):251–267

Auroux D, Masmoudi M (2008) Image processing by topological asymptotic expansion. J Math Imaging Vis 33(2):122

Baghaie A, Zeyun Y (2015) Structure tensor based image interpolation method. AEU Int J Elect Commun 69(2):515–522

Batchelor PG, Moakher M, Atkinson D, Calamante C, Connelly A (2005) A rigorous framework for diffusion tensor calculus. Magn Reson Med 53(1):221–225

Ben Haddouch K, El Allali Z, Tsouli N, El Habib S, Kissi F (2016) Existence of solutions for a fourth order eigenvalue problem with variable exponent under Neumann boundary conditions. Bol Soc Paran Math 34(1):253–272

Bertozzi A, Schönlieb C-B (2011) Unconditionally stable schemes for higher order inpainting. Commun Math Sci 9(2):413–457

Bredies K, Kunisch K, Pock T (2010) Total generalized variation. SIAM J Imaging Sci 3(3):492–526

Chan T, Marquina A, Mulet P (2000) High-order total variation-based image restoration. SIAM J Sci Comput 22(2):503–516

Ciarlet PG, Dinca G, Matei P (2013) Fréchet differentiability of the norm in a sobolev space with a variable exponent. Anal Appl 11(04):1350012

Diening L, Harjulehto P, Hästö P, Ruzicka M (2011) Lebesgue and Sobolev spaces with variable exponents. Springer, Berlin

Drogoul A (2016) Numerical analysis of the topological gradient method for fourth order models and applications to the detection of fine structures in imaging. SIAM J Imaging Sci 7(4):2700–2731

Edmunds DE, Rákosník J (2000) Sobolev embeddings with variable exponent. Stud Math 143(3):267–293

El Amrouss AR, Ourraoui A (2012) Existence of solutions for a boundary problem involving p (x)-biharmonic operator. Boletim da sociedade paranaense de matemática 31(1):179–192

El Amrouss A, Moradi F, Moussaoui M (2009) Existence of solutions for fourth-order PDEs with variable exponents. Electron J Differ Equ 2009(153):1–13

Elsey M, Wirth B (2013) A simple and efficient scheme for phase field crystal simulation. ESAIM Math Model Numer Anal 47(5):1413–1432

Eyre DJ (1998) An unconditionally stable one-step scheme for gradient systems. Unpublished article

Fan X, Zhao D (2001) On the spaces $L^{p(x)}$ and $W^{m,p(x)}$. J Math Anal Appl 263(2):424–446

Fillard P, Arsigny V, Ayache N, Pennec X (2005) A riemannian framework for the processing of tensor-valued images. In: International Workshop on Deep Structure, Singularities, and Computer Vision, pages 112–123. Springer

Heidarkhani S, Afrouzi GA, Moradi S, Caristi G, Ge B (2016) Existence of one weak solution for $p(x)$-biharmonic equations with navier boundary conditions. Zeitschrift für angewandte Mathematik und Physik 67(3):73

Houichet H, Moakher M, Rjaibi B (2019) Noise removal and edge detection in ultrasound images by the topological gradient method. New Trends Math Sci 7(4):421–440

Houichet H, Theljani A, Rjaibi B, Moakher M (2019) A nonstandard higher-order variational model for speckle noise removal and thin-structure detection. J Math Study 52(4):394–424

Houichet H, Theljani A, Mohamed A (2019) Well-posedness of high-order non-standard parabolic partial differential equation for image denoising. Submitted, page 25

Jaafar Belaid L, Jaoua M, Masmoudi M, Siala ML (2008) Application of the topological gradient to image restoration and edge detection. Eng Anal Bound Elements J 32(11):891–899

Jin Z, Yang X (2011) A variational model to remove the multiplicative noise in ultrasound images. J Math Imaging Vis 39(1):62–74

Kim J, Shin J (2017) An unconditionally gradient stable numerical method for the Ohta–Kawasaki model. Bull Korean Math Soc 54(1):145–158

Krissian K, Kikinis R, Westin CF, Vosburgh K (2005) Speckle-constrained filtering of ultrasound images. In: 2005 IEEE Computer Society Conference on Computer Vision and Pattern Recognition (CVPR'05), 2:547–552

Michael H, Michael H, Hicham TM (2011) An adaptive finite-element Moreau–Yosida-based solver for a non-smooth Cahn–Hilliard problem. Optim Methods Softw 26(4–5):777–811

Prasath VBS, Vorotnikov D, Pelapur R, Jose S, Seetharaman G, Palaniappan Kannappan (2015) Multiscale tikhonov-total variation image restoration using spatially varying edge coherence exponent. IEEE Trans Image Process 24(12):5220–5235

Rudin LI, Osher S, Fatemi E (1992) Nonlinear total variation based noise removal algorithms. Physica D Nonlinear Phenom 60(1):259–268

Stuart AM, Humphries AR (1994) Model problems in numerical stability theory for initial value problems. SIAM Rev 36(2):226–257

Surya Prasath VB (2016) Adaptive coherence-enhancing diffusion flow for color images. Informatica 40(3):337

Theljani A (2020) Multi-scale non-standard fourth-order pde in image denoising and its fixed point algorithm. Int J Numer Anal Model

Theljani A, Belhachmi Z, Moakher M (2019) High-order anisotropic diffusion operators in spaces of variable exponents and application to image inpainting and restoration problems. Nonlinear Anal Real World Appl 47:251–271

Weickert J, Scharr H (2002) A scheme for coherence-enhancing diffusion filtering with optimized rotation invariance. J Vis Commun Image Represent 13(1–2):103–118

Yuille AL, Rangarajan A (2003) The concave-convex procedure. Neural Computat 15(4):915–936